Stockholm University

# Bachelor Thesis

Degree Project in
Geological Science, 15 hp

# Characterizing deformation microstructures of eclogites from Holsnøy, western Norway

Aleksandar Jerkovic

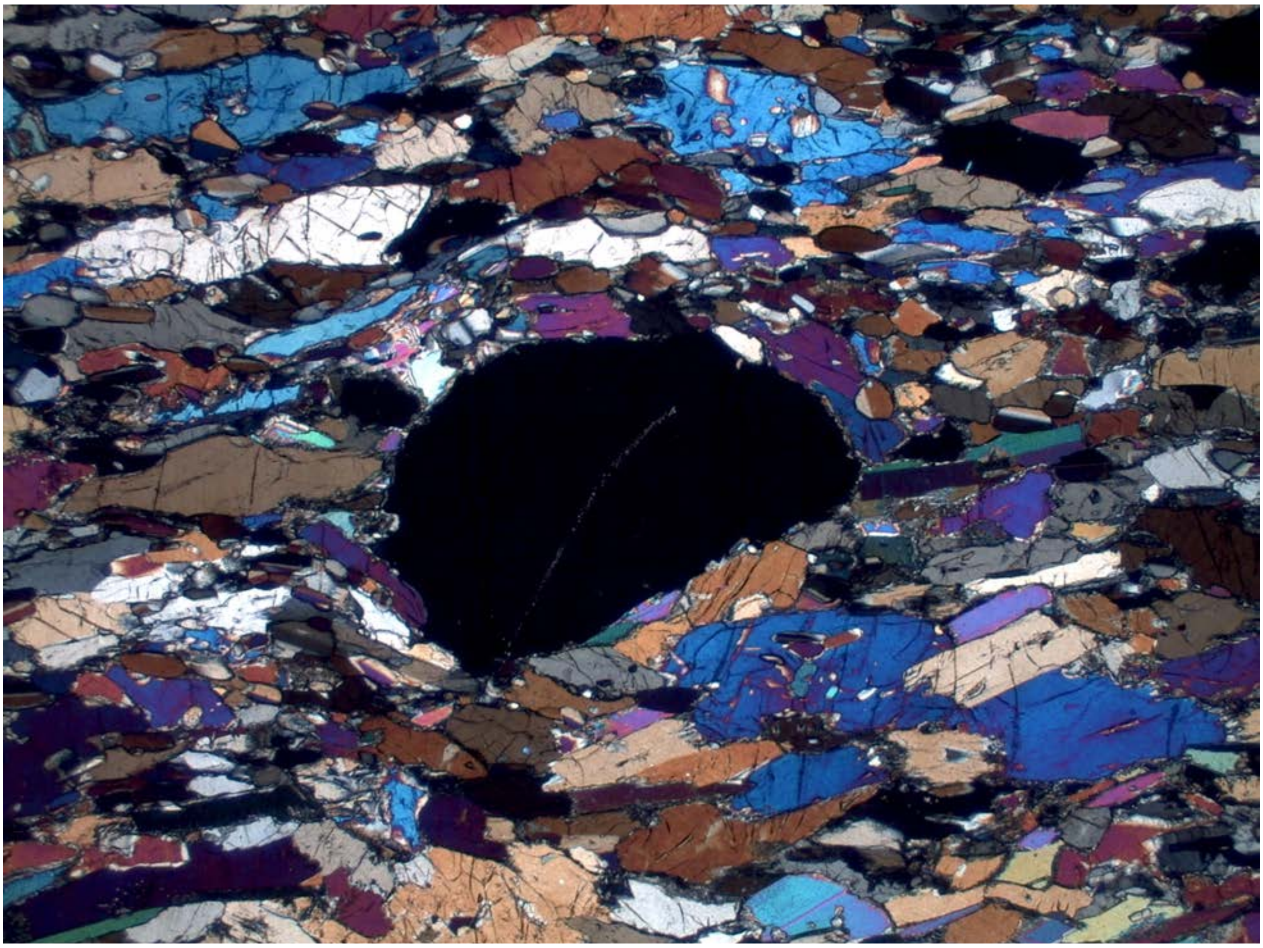

Stockholm 2026

Department of Geological Sciences
Stockholm University
SE-106 91 Stockholm

# Abstract

Eclogites from Holsnøy, western Norway, preserve evidence for the interaction between metamorphic reactions, fluid infiltration and deformation in deeply buried lower crust. This study characterizes deformation microstructures in Holsnøy eclogites using optical microscopy and scanning electron microscopy (SEM) including electron backscatter diffraction (EBSD), with the aim of evaluating the dominant deformation mechanism. Three samples were studied by optical microscopy, two by SEM, and one by EBSD. The samples are dominated by garnet and omphacite rich eclogite-facies assemblages with variable foliation intensity, compositional banding and local retrograde modification. Omphacite forms the main matrix phase and defines much of the foliation. EBSD data from one sample show that omphacite has a crystallographic preferred orientation (CPO), however, grain reference orientation deviation (GROD) and grain orientation spread (GOS) maps show generally low internal misorientation in omphacite. Low angle boundaries are rare, and evidence for subgrain development is limited. In contrast, quartz shows undulose extinction and subgrain development with local internal misorientation. These observations do not support dominant dislocation creep as the main deformation mechanism in omphacite. Instead, the microstructures are more consistent with diffusion assisted or dissolution-precipitation assisted deformation during eclogite-facies recrystallization, probably accompanied by grain boundary sliding (GBS), with possible minor or local dislocation creep. The results show that omphacite SPO and CPO alone should not be interpreted as direct evidence for dislocation creep, and that crystallographic data should be combined with microstructural observations when interpreting deformation mechanisms in eclogite-facies rocks.



**Keywords:** Holsnøy eclogites, microstructures, deformation mechanisms, omphacite, EBSD, dislocation creep, diffusion creep

# Table of Contents

# 1. Introduction

Eclogites are high-pressure metamorphic rocks that commonly form during subduction and continental collision from mafic protoliths such as basalt, gabbro and granulite (Jamtveit et al., 1990; Rogowitz and Huet, 2021). Because eclogites may occur in subducted oceanic crust and lower continental crust, they provide important information about metamorphism, deformation, fluid-rock interaction and exhumation at great depth (Park and Jung, 2019). Understanding how eclogites form and deform is therefore important for interpreting the mechanical behaviour of convergent plate boundaries and deeply buried crustal rocks.

The metamorphism of mafic rocks into eclogite-facies assemblages is strongly influenced by fluids. Although the typical eclogite mineral assemblage consists of garnet and omphacite, fluid infiltration is generally required to initiate and sustain metamorphic reactions under high-pressure conditions (Jamtveit et al., 1990; Rogowitz and Huet, 2021). Fluids can promote dissolution, element transport and precipitation of new mineral phases. However, the exact role remains debated, especially whether fluids mainly speed up reactions or also change the local chemical conditions during metamorphism (Rogowitz and Huet, 2021). Fluid pathways are commonly linked to brittle deformation, such as fractures, which may evolve into ductile shear zones that localize deformation and channelize fluid flow (Kaatz et al., 2021; Zertani et al., 2019). These processes can generate transient porosity, reduce grain size, and promote the development of weaker, hydrated mineral assemblages, resulting in significant rock weakening (Kaatz et al., 2021; Rogowitz and Huet, 2021; Zertani et al., 2022).

Eclogitization may be closely linked to deformation, but the relationship between reaction and strain is not always simple. Zertani et al. (2019) showed that fluid mediated eclogitization on Holsnøy may occur both dynamically within shear zones and more statically in less deformed domains. This means that eclogite-facies metamorphism does not only depend on deformation intensity, but also on where fluids were able to enter the rock.  In many natural systems, these processes operate together, resulting in a complex interplay between fluid flow, metamorphic reactions and strain localization (Zertani et al., 2019). These transformations also affect the physical properties of rocks, including density, rigidity, and seismic behaviour, which are controlled by mineral assemblages and microstructures (Park and Jung, 2019).

The deformation mechanisms operating in eclogites remain a subject of ongoing debate and are closely related to microstructural development. Deformation may occur through dislocation creep, diffusion creep, brittle fracturing or dissolution-precipitation processes, depending on factors such as pressure, temperature, grain size, mineralogy and fluid availability (Vernon, 2004; Passchier and Trouw, 2005; Stünitz et al., 2020; McNamara et al., 2024). Microstructural analysis is therefore important for identifying deformation mechanisms, because features such as foliation, shape preferred orientation (SPO), crystallographic preferred orientation (CPO), grain size variation, subgrains, misorientation patterns and reaction textures provide information about how strain was accommodated (Passchier and Trouw, 2005; McNamara et al., 2024). However, these features must be interpreted carefully, because similar microstructures can form by different processes. In particular, CPO in omphacite may indicate dislocation creep, but Stünitz et al. (2020) and McNamara et al. (2024) showed that strong omphacite fabrics can also form during mineral growth, dissolution-precipitation, or diffusion-assisted deformation. In addition, retrograde reactions, such as the breakdown of omphacite into symplectic intergrowths and the formation of amphibole, can modify earlier microstructures during exhumation (Zertani et al., 2024). Dutta et al. (2026) further showed that omphacite breakdown and symplectite formation can preserve inherited crystallographic relationships while also recording different deformation mechanisms in different reaction products.

## 2. Aim of the Study

This study investigates deformation microstructures in eclogites from Holsnøy, western Norway, using optical microscopy and scanning electron microscopy (SEM) including electron backscatter diffraction (EBSD). The aim is to characterize the microstructures of selected eclogite thin sections and evaluate the deformation mechanisms, with particular focus on omphacite as the dominant fabric forming phase. The results are compared with recent literature on deformation mechanisms in eclogites.

## 3. Geological Setting

The study area is located on the island of Holsnøy in the Bergen Arcs of western Norway (Figure 1). The Bergen Arcs formed during the Scandian phase of the Caledonian orogeny as a result of the collision between Baltica and Laurentia after the closure of the Iapetus Ocean (Zertani et al., 2019; Kaatz et al., 2021). The Bergen Arcs consist of a curved nappe complex that was thrust southeastwards onto Baltica during the Caledonian collision. These nappes include material derived from both the former Iapetus Ocean and the pre-Caledonian margin of Baltica (Zertani et al., 2019). The rocks exposed on Holsnøy belong to the Lindås Nappe, which represents part of the pre-Caledonian lower continental crust (Bhowany et al., 2018; Zertani et al., 2019).

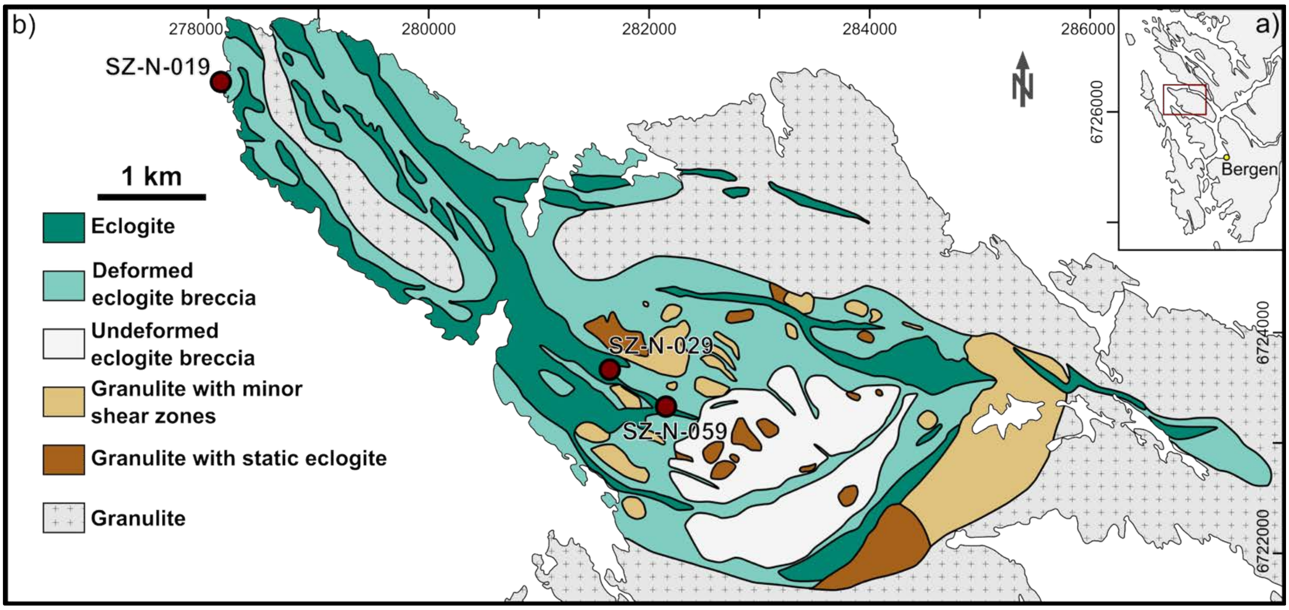


*Figure 1: Geological setting of Holsnøy in the Bergen Arcs, western Norway, showing the locations of studied samples. Modified after Zertani et al. (2022).*

The Lindås Nappe is mainly composed of anorthositic and gabbroic rocks that were metamorphosed under granulite-facies conditions before Caledonian burial (Zertani et al., 2019). During the Caledonian orogeny, these lower crustal rocks were buried to eclogite-facies conditions at approximately 430 Ma (Zertani et al., 2019; Kaatz et al., 2021). Peak eclogite-facies conditions are generally estimated at 1.7-2.1 GPa and 650-750 °C (Bhowany et al., 2018; Zertani et al., 2022). The eclogite facies assemblages commonly include garnet, omphacite, zoisite or clinozoisite, phengite, kyanite, rutile and quartz (Zertani et al., 2019). Eclogitization on Holsnøy is spatially heterogeneous and strongly controlled by fluid infiltration (Jamtveit et al., 1990; Zertani et al., 2019). Large parts of the dry granulite protolith remained only weakly affected, whereas areas infiltrated by fluids were partially or completely transformed into eclogite. This produced a mixture of preserved granulite, eclogite breccia, eclogite veins and deformed eclogite-facies shear zones. The preservation of both granulite and eclogite on Holsnøy makes the area especially useful for studying the relationship between fluid infiltration, metamorphic reaction and deformation (Zertani et al., 2019). Fluids are thought to have entered the rocks along fractures generated during brittle deformation and were later channelized along ductile shear zones, where metamorphic reactions were concentrated. Once reactions began, the newly formed eclogite was weaker than the surrounding granulite and therefore more likely to localize ductile deformation (Kaatz et al., 2021). However, eclogitization on Holsnøy did not only occur in strongly deformed shear zones. Zertani et al. (2019) showed that fluid mediated eclogitization also occurred statically in less deformed domains. As a result, Holsnøy preserves both dynamically eclogitized shear zones and less deformed domains where the granulite-facies structure may still be preserved despite eclogite-facies mineral replacement (Zertani et al., 2019). After peak eclogite-facies metamorphism, the rocks were partly overprinted during exhumation under amphibolite-facies conditions. This retrogression occurred at approximately 0.8-1.0 GPa and around 600 °C, and retrograde reactions may have modified some earlier eclogite-facies microstructures (Bhowany et al., 2018).

# 4. Methods

### 4.1 Optical Microscopy

A total of 11 thin sections from eclogites on Holsnøy, western Norway, were provided for this study. Initial observations were carried out on all thin sections using a Leica DMLP transmitted light optical microscope in the graduate microscopy laboratory at Stockholm University. The thin sections were examined in both plane polarized light (PPL) and crossed polarized light (XPL) in order to identify mineral phases and describe the microstructures.

Based on the initial observations, three samples, SZ-N-019, SZ-N-029 and SZ-N-059, were selected for detailed analysis. The locations of these samples are shown in Figure 1. These samples were chosen because they were well preserved and contained mineral assemblages and microstructures relevant to the aims of the study, such as garnet and omphacite rich assemblages, foliation, compositional banding and reaction textures. They also allowed comparison between different microstructural domains, including weakly to strongly foliated domains and reaction related features. The petrographic analysis focused on mineral assemblage, grain size, grain shape, grain boundary geometry, foliation development, phase relationships and reaction microstructures. Photomicrographs were taken using a Leica EC3 camera attached to the microscope and controlled with Leica Acquire software. Images were taken at 2.5x, 10x and 20x magnification. The remaining thin sections were not studied in detail because they were less suitable for the aims of the study, either due to lower thin section quality, less clearly developed microstructures or less representative deformation features.

#### *4.1.2 Grain size measurements*

Grain size measurements were carried out using Leica Acquire software on representative photomicrographs. For each selected sample, approximately 20 grains from representative mineral phases were measured. Grain size was measured along the longest axis of each grain. The measurements were used to estimate average grain size and compare grain size differences between samples.

**4.2 Scanning Electron Microscopy (SEM)**

Two samples, SZ-N-029 and SZ-N-059, were selected for scanning electron microscopy (SEM) analysis. These samples were chosen based on their well developed and representative microstructures observed during optical microscopy, including foliation, grain size variation, compositional banding and reaction textures. Sample preparation and SEM analysis were carried out at the Swedish Museum of Natural History (Naturhistoriska riksmuseet), Stockholm. Before SEM analysis, the thin sections were cleaned, dried and carbon-coated using a BAL-TEC CED 030 carbon evaporator to ensure electrical conductivity and improve imaging quality. SEM imaging was performed using a Quanta FEG 650 scanning electron microscope. Backscattered electron (BSE) imaging and energy-dispersive X-ray spectroscopy (EDS) were used to identify mineral phases and examine grain boundaries, phase relationships and microstructures not resolvable by optical microscopy.

**4.3 Electron Backscatter Diffraction (EBSD)**

After the initial SEM investigation and mineral identification, the thin sections were repolished to obtain a suitable surface for EBSD analysis. Polishing was first carried out using AKA-Spray Poly 0.25 µm and then with a colloidal silica suspension. The samples were then cleaned and dried for a few minutes at 40 °C. After polishing, the thin sections were coated again using a thin carbon coat.

EBSD is a technique used to determine the crystallographic orientation of minerals. During analysis, an electron beam interacts with a polished and tilted crystalline surface and produces backscattered electron diffraction patterns, known as Kikuchi patterns. These patterns are collected by the EBSD detector and indexed by the software, allowing the crystallographic orientation of individual measurement points to be determined. EBSD was used to examine crystallographic preferred orientation (CPO), phase distribution, grain boundary relationships, and internal misorientation within grains. The EBSD map was acquired from sample SZ-N-059 using AZtec software at an accelerating voltage of 20 kV, a working distance of 19 mm, and a step size of 3.5 µm, which required approximately 10 h of acquisition time. The sample was tilted to 70° relative to the electron beam, as this high angle increases the number of backscattered electrons reaching the detector and improves the quality of the diffraction patterns. The EBSD dataset was processed using AztecCrystal software. During processing, the autoclean function was applied to reduce misindexed pixels and improve map readability. Phase maps, inverse pole figure (IPF) maps, grain reference orientation deviation (GROD) maps and grain orientation spread (GOS) maps were generated. Phase maps were used to show the distribution of indexed minerals. IPF maps were used to show crystallographic orientation variations between grains. GROD and GOS maps were used to evaluate internal misorientation and the degree of intragranular deformation. For grain boundary analysis, low angle boundaries were defined as 2-10°, whereas high angle boundaries were defined as >10°.

In the EBSD output, clinopyroxene was indexed as diopside, garnet as pyrope and white mica as muscovite. Based on optical microscopy and EDS analysis, these phases are referred to in this thesis as omphacite, garnet and phengite, respectively. The EBSD interpretation focused mainly on omphacite because it is the dominant matrix phase and was indexed most reliably. Quartz was also examined where indexing quality allowed, but its EBSD data are used as supporting evidence only. Kyanite and clinozoisite were less reliably indexed and are therefore not used for detailed deformation mechanism interpretation. Some parts of the EBSD dataset were affected by indexing difficulties and noise. These limitations were considered during interpretation, and anomalous data with holes in the sample or poorly indexed areas were excluded where necessary. The thin section was cut parallel to lineation and perpendicular to foliation. Therefore, the EBSD X direction corresponds to the structural lineation, whereas the EBSD Y direction corresponds to the foliation normal. This orientation was considered when comparing the pole figures with published data.

# 5. Results

## 5.1 Optical Microscopy

### *5.1.1. SZ-N-019*

Sample SZ-N-019 is composed mainly of garnet and omphacite, with subordinate clinozoisite and minor amphibole and rutile. The sample has an inequigranular microstructure, with coarse grained garnet grains and aggregates set in a finer grained omphacite rich matrix (Figure 2).

Garnet occurs as coarse, inclusion rich grains and aggregates. In some domains, garnet forms clustered networks extending over several millimeters (Figure 3a). Many garnet grains are fractured and contain inclusions of matrix minerals and rutile. Omphacite forms the dominant matrix phase. It occurs as fine to medium grained grains that are generally subhedral to anhedral and slightly elongated. This alignment defines a weak foliation (Figure 3b). Two grain size domains are present, a coarser domain with an average grain size of 0.75 mm and a finer grained domain with an average grain size of 0.15 mm (Appendix A, Table A 1). Clinozoisite occurs as a subordinate matrix phase with elongate to irregular grain shapes. Some grains show optically distinct core and rim domains (Figure 3c). Amphibole occurs as a minor phase and is commonly associated with omphacite. Some amphibole grains show undulose extinction and irregular to lobate grain boundaries against adjacent omphacite (Figure 3d,e). Rutile occurs as small, high relief grains and is commonly present as inclusions within garnet.

The matrix is locally polygonal, especially in omphacite-rich domains where grain boundaries are relatively straight and triple junctions approach 120° (Figure 3f). In other areas, grain boundaries are more irregular to lobate. Fine symplectic intergrowths occur locally along some grain boundaries.

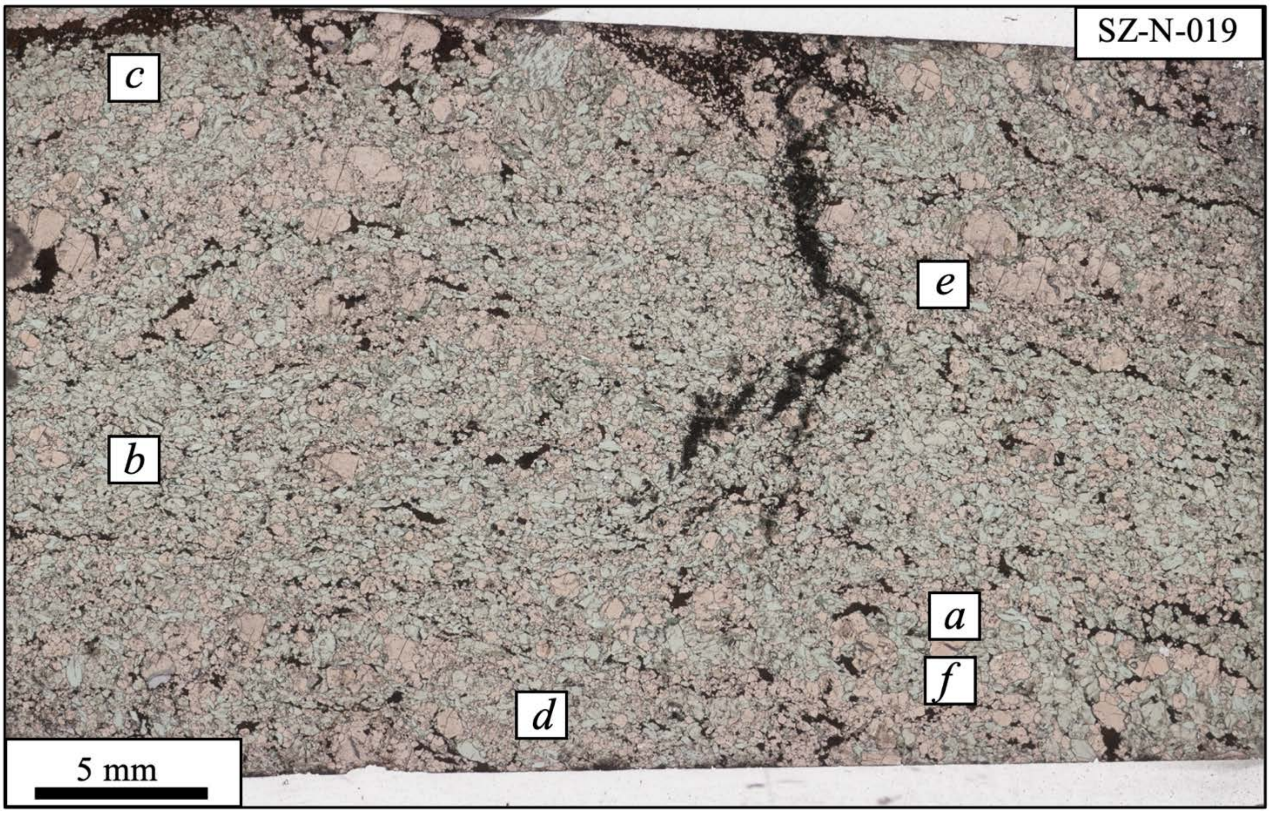


*Figure 2: Whole thin section view in PPL. Boxes labelled a-f show the locations of the detailed micrographs from figure 3.*

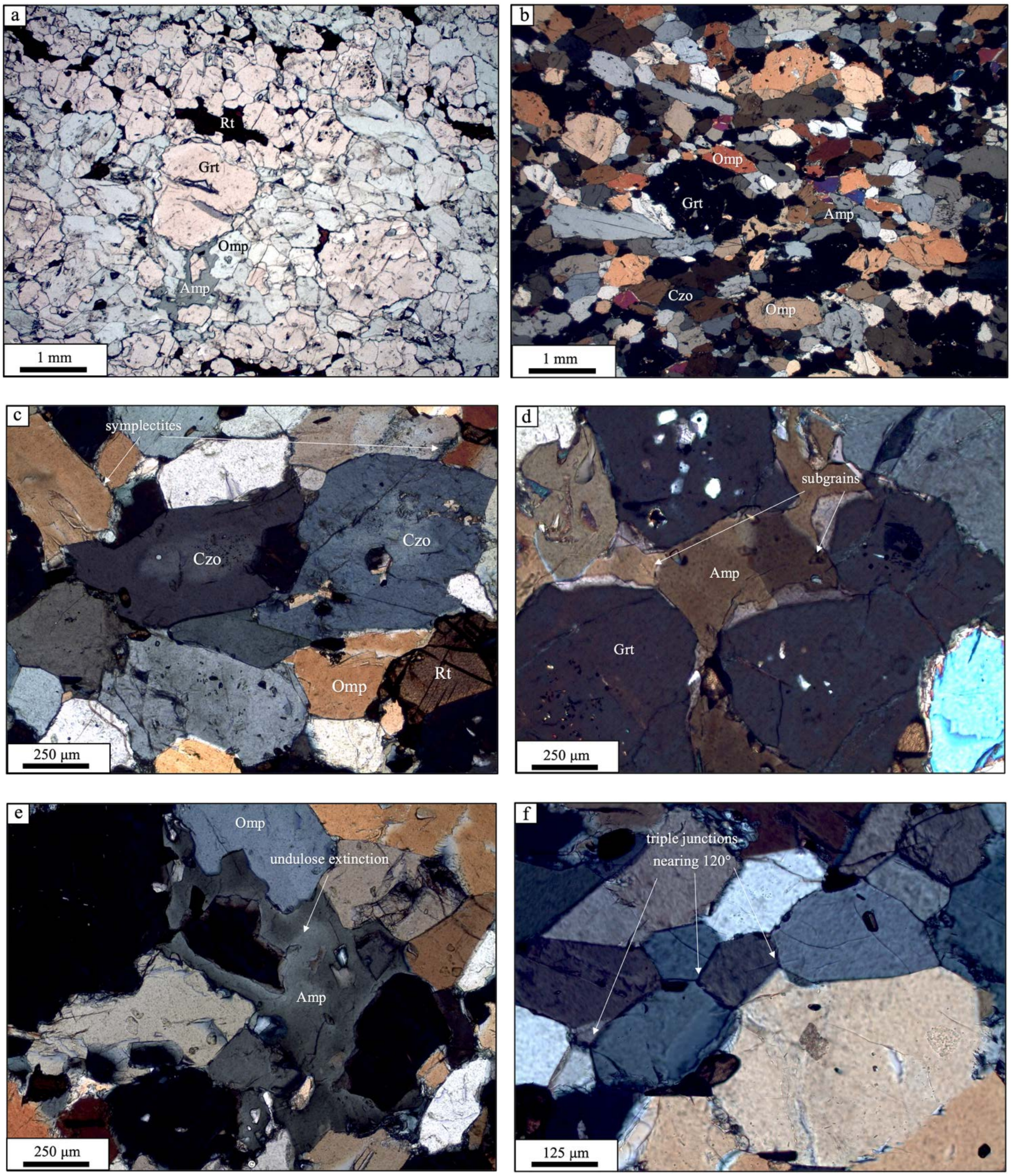


*Figure 3: Optical microstructures of sample SZ-N-019: (a) Garnet aggregate in PPL showing inclusion-rich garnet in an omphacite rich matrix. (b) Omphacite rich matrix domain in XPL. (c) Zoned clinozoisite in XPL associated with local fine intergrowths along grain boundaries. (d) Amphibole grain in XPL showing internal extinction variation. (e) Amphibole grain in XPL showing undulose extinction and an irregular to lobate phase boundary with adjacent omphacite. (f) Omphacite-rich domain in XPL with straight grain boundaries and triple junctions approaching 120°.*

*5.1.2 SZ-N-029*

Sample SZ-N-029 consists mainly of garnet, omphacite, kyanite and clinozoisite with minor phengite, amphibole and rutile. The sample displays a strongly foliated microstructure defined by elongate matrix grains. The matrix also shows compositional banding, with alternating omphacite rich and clinozoisite-kyanite rich domains (Figure 4).

Garnet occurs as coarse porphyroblasts, some of which are inclusion rich (Figure 5a,b). Matrix minerals adjacent to larger garnets are deflected and produce curvature of the surrounding foliation (Figure 5b). Omphacite is the main matrix phase and occurs as elongate grains that define a strong shape preferred orientation (SPO) (Figure 5a,b). Omphacite rich domains form relatively continuous layers within the foliated matrix. Kyanite occurs as fine grained, commonly rounded grains, mainly in kyanite-clinozoisite rich bands (Figure 5c,d). Some grains show straight internal features interpreted as simple twinning. Clinozoisite occurs as coarser elongate grains commonly associated with kyanite in the same bands (Figure 5c,e). Some clinozoisite grains show undulose extinction and local internal optical variation (Figure 5e). Amphibole occurs near grain boundaries or as inclusions within garnet (Figure 5a). Some grains show undulose extinction. Phengite occurs as elongate, platy matrix phase. Rutile occurs as a minor high relief phase.

Grain boundaries in the matrix are commonly irregular and are often associated with fine symplectic intergrowths (Figure 5e). In some coarser domains, grain boundaries are more regular and some triple junctions approach 120°. Grain size measurements show that omphacite grains are relatively coarse, with average grain sizes of approximately 1 mm, whereas kyanite occurs as a distinctly finer grained phase with an average grain size of 0.13 mm. Garnet grains are larger overall, with an average grain size of 1.6 mm (Appendix A, Table A 2). Overall, SZ-N-029 is characterized by strong foliation, elongate omphacite grains, compositional banding, irregular to locally polygonal grain boundaries, and fine intergrowths along matrix grain boundaries (Figure 4).

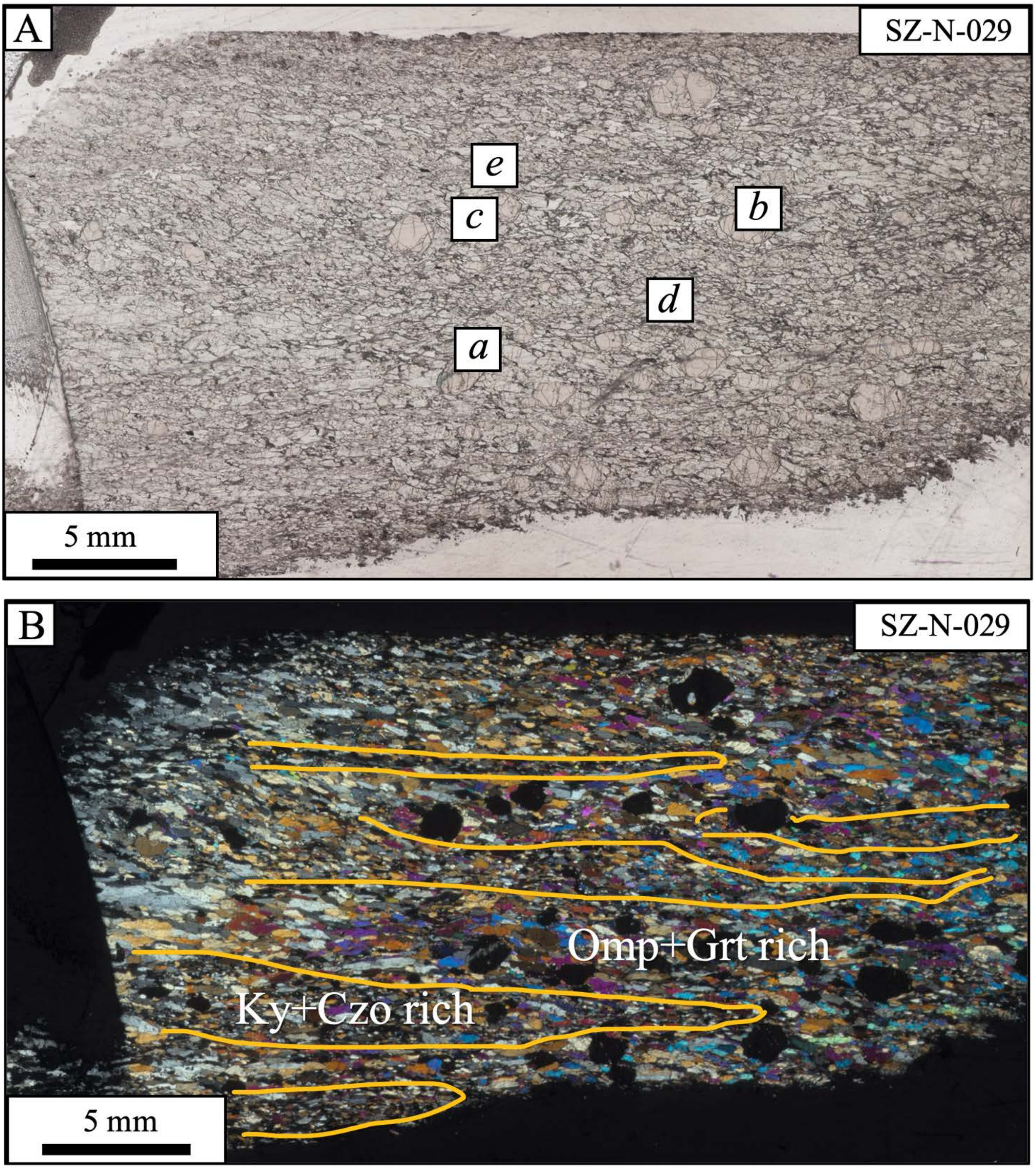


*Figure 4: (A) Whole thin section view in PPL. Labels a-e show the locations of detailed micrographs from figure 5. (B) Whole thin section in XPL showing compositional banding with kyanite-clinozoisite and omphacite-garnet rich domains.*

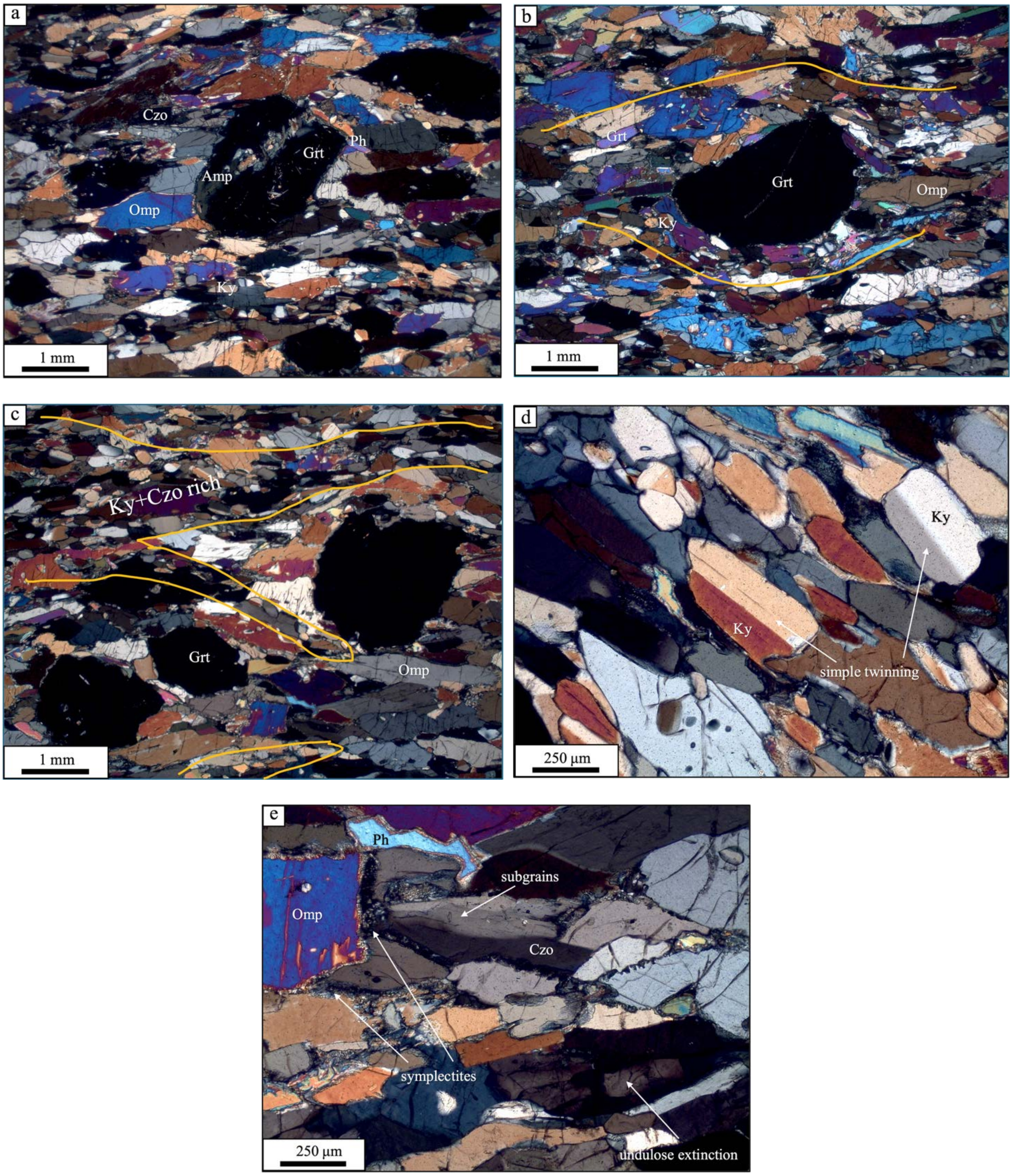


*Figure 5: Optical microstructures of sample SZ-N-029: (a) XPL image showing elongate omphacite in the matrix and garnet containing amphibole rich inclusions. (b) XPL image showing elongated matrix grains deflected around the garnet. (c) XPL image of a kyanite-clinozoisite rich band. (d) XPL image showing kyanite grains with simple twinning. (e) XPL image showing fine intergrowths and clinozoisite with internal extinction variation.*

*5.1.3. SZ-N-059*

Sample SZ-N-059 contains garnet, omphacite, clinozoisite, kyanite and quartz, with minor phengite, amphibole and rutile. The sample displays a foliated microstructure defined mainly by elongate matrix grains. Weak compositional banding is also present, with omphacite rich and clinozoisite-kyanite rich domains (Figure 6).

Garnet occurs as coarse grains, some of which contain inclusions (Figure 7a). Omphacite occurs as elongate matrix grains and contributes strongly to the foliation (Figure 7a). Some omphacite grains show internal variation in interference colours under XPL, with blue cores and orange to white rims (Figure 7f). Clinozoisite occurs as elongate to irregular matrix grains. Some grains show undulose extinction and local optical zoning (Figure 7b). Kyanite occurs as fine grained, commonly rounded grains often displaying simple twinning (Figure 7a). Phengite occurs as an elongate, platy matrix phase. Amphibole is present along garnet margins and as inclusions within garnet. Rutile is present as a minor, high relief phase. Quartz occurs as relatively coarse grains. Quartz grains commonly have irregular to lobate phase boundaries against adjacent omphacite (Figure 7c,e). Many quartz grains display undulose extinction and contain abundant subgrains (Figure 7d,f).

Grain and phase boundaries throughout the sample are generally irregular. Fine symplectic intergrowths occur locally, especially along omphacite grain boundaries (Figure 7c). Grain size measurements show an average omphacite grain size of approximately 0.8 mm, whereas kyanite is finer grained, with an average grain size of 0.18 mm. Quartz grains are coarse, with an average grain size of 1.14 mm, and garnet grains have an average grain size of 1.24 mm (Appendix A, Table A 3).
Overall, SZ-N-059 is characterized by a foliated omphacite rich matrix, weak compositional banding, irregular phase boundaries, coarse quartz domains and local fine intergrowths along grain boundaries.

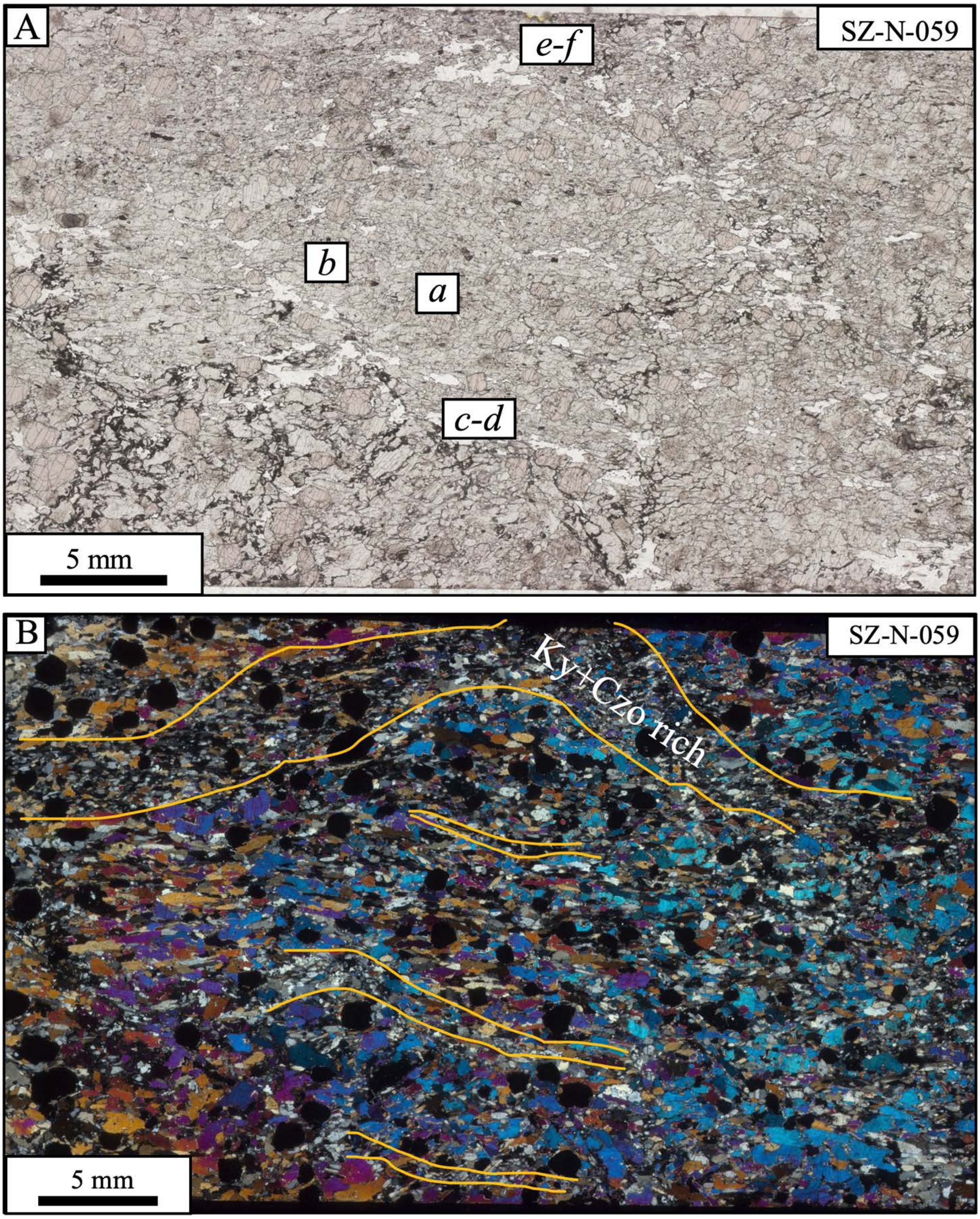


*Figure 6: (A) Whole thin section view in PPL. Labels b-g show the locations of the detailed micrographs from figure 7. (B) Whole thin section in XPL showing irregular compositional banding defined by kyanite-clinozoisite rich bands.*

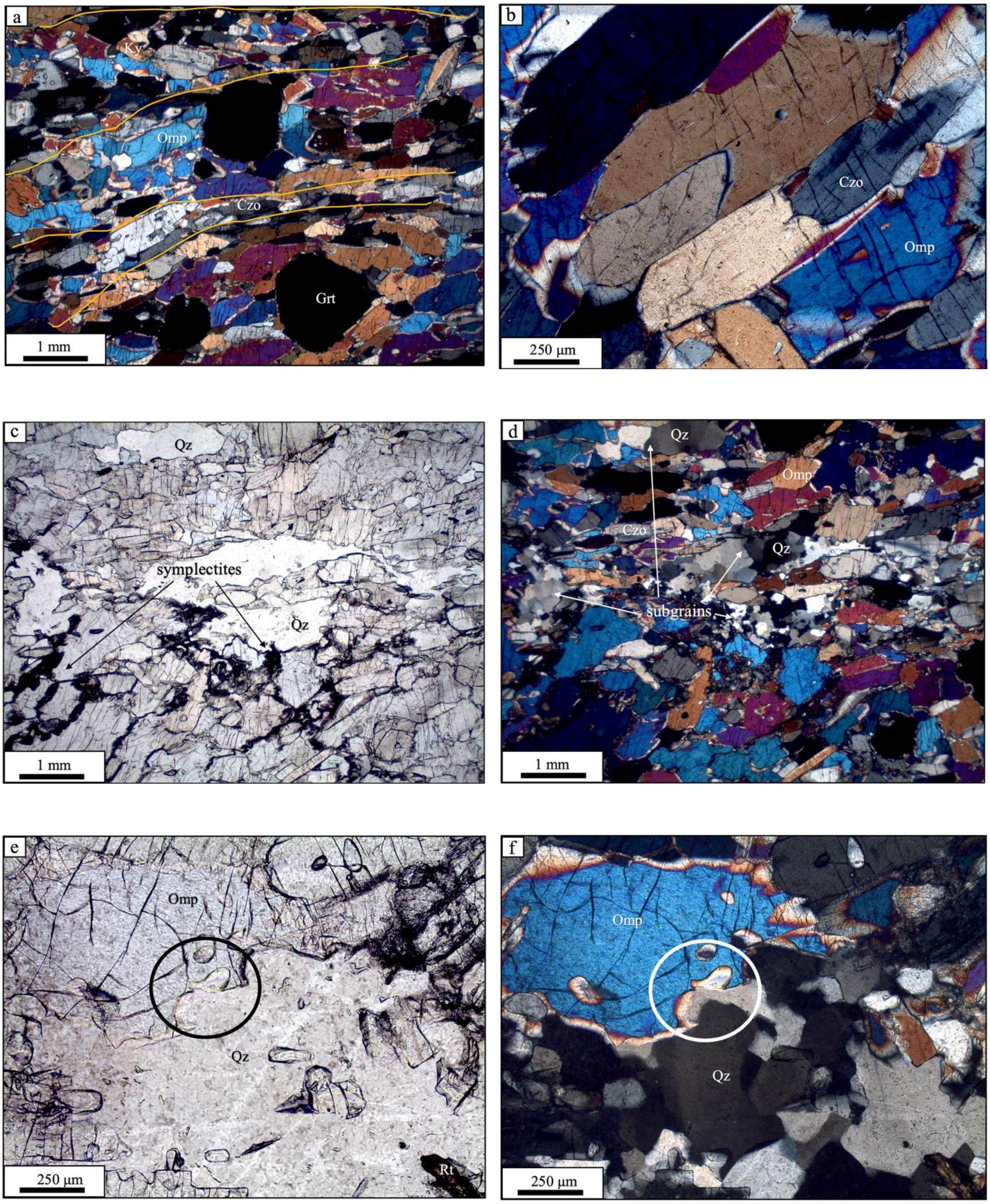


*Figure 7: Optical microstructures of sample SZ-N-059: (a) XPL image showing elongate omphacite grains defining the foliation, weak compositional banding and kyanite grains with simple twinning. (b) Zoned clinozoisite grain in XPL. (c) Quartz-rich domain in PPL with fine intergrowths. (d) Same domain in XPL showing quartz grains with abundant subgrains. (e) PPL image of a lobate phase boundary between omphacite and quartz. (f) Same omphacite-quartz boundary and internal variation in interference colours in omphacite grain in XPL.*

## 5.2. Scanning Electron Microscopy (SEM)

*5.2.1. SZ-N-029*

Backscattered electron (BSE) imaging and energy-dispersive X-ray spectroscopy (EDS) of sample SZ-N-029 confirm the presence of garnet, omphacite, kyanite, clinozoisite, phengite and amphibole (Appendix B, Table B 1). The sample shows a strongly foliated microstructure defined by elongate matrix grains and compositional banding between omphacite rich and kyanite-clinozoisite rich domains (Figure 9a). Garnet occurs as coarse grains and displays compositional zoning expressed by darker cores and brighter rims (Figure 9a,b). Chemical data show that the garnet rims are relatively Fe-rich and Mg-poor compared with the cores (Figure 8; Appendix B, Table B 3). Garnet boundaries are typically irregular to lobate, and fine grained intergrowths occur along some garnet margins. The matrix is dominated by elongate omphacite grains, together with kyanite and clinozoisite rich domains (Figure 9a). Omphacite rich layers form relatively continuous parts of the foliated matrix. Many omphacite grain boundaries are generally straight and are often difficult to distinguish. Fine symplectic intergrowths occur mainly along omphacite grain boundaries. No clear intracrystalline deformation features were observed in omphacite. Kyanite and clinozoisite occur together in compositionally distinct bands, confirming the phase distribution observed by optical microscopy. Phengite and amphibole occur as minor phases (Figure 9c).

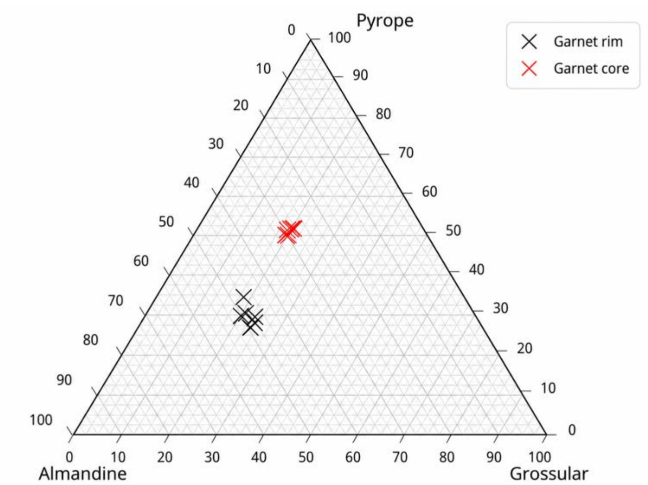


*Figure 8: Ternary diagram showing garnet compositions from sample SZ-N-029 plotted in the Alm-Prp-Grs system. Garnet cores plot at relatively higher pyrope contents, whereas garnet rims are shifted toward relatively higher almandine contents. The rims are Fe-richer and Mg-poorer relative to the cores.*

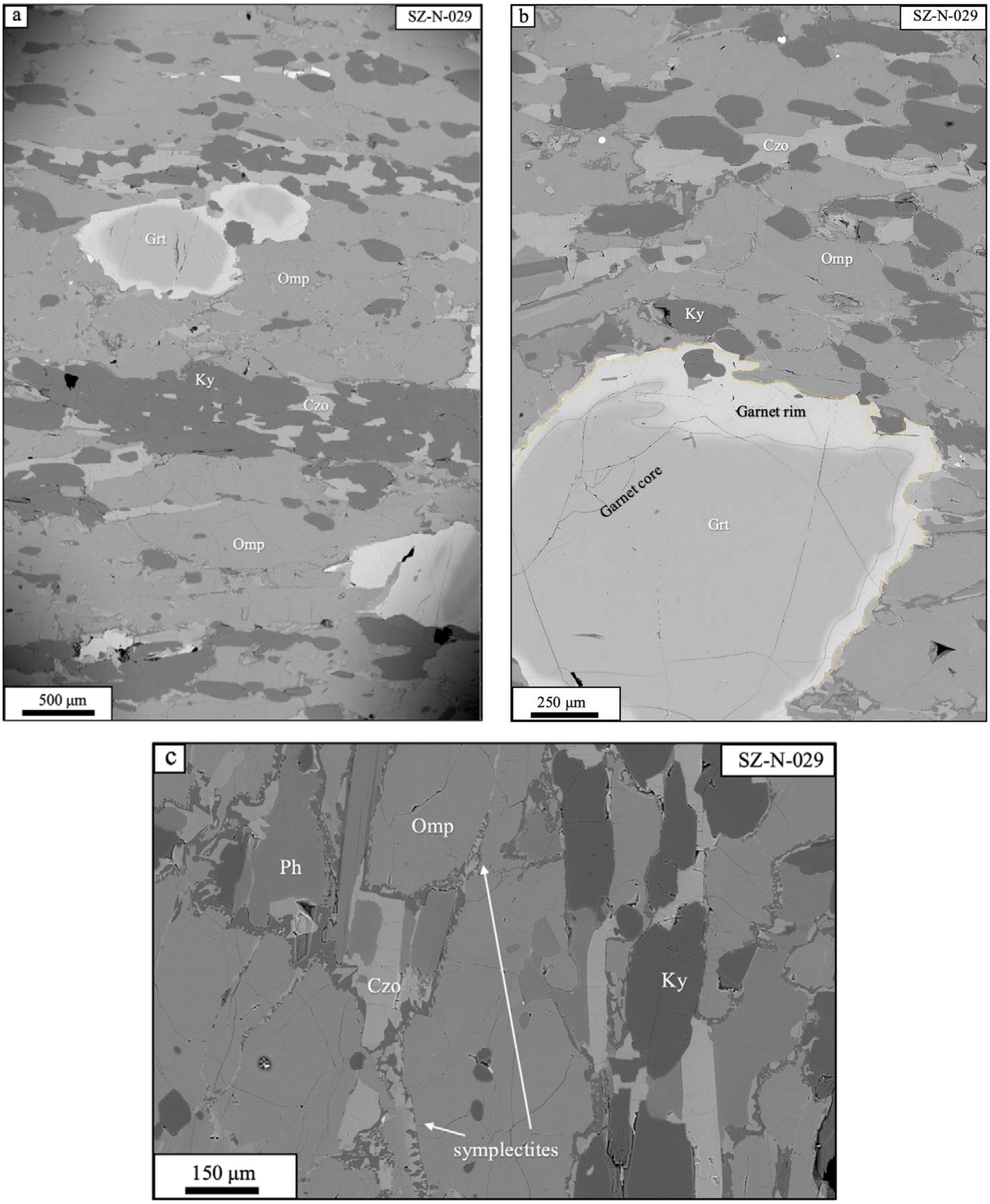


*Figure 9: BSE images of sample SZ-N-029. (a) Overview image showing the foliated matrix and compositional banding with ky-czo rich domains in an omphacite rich matrix. (b) Zoned garnet with a darker core, brighter rim and irregular grain boundary. (c) Matrix domain containing kyanite, omphacite, phengite and clinozoisite, with fine symplectic intergrowths developed along grain boundaries.*

*5.2.2. SZ-N-059*

Backscattered electron (BSE) imaging and energy-dispersive X-ray spectroscopy (EDS) analysis of sample SZ-N-059 confirm the presence of garnet, omphacite, clinozoisite, kyanite and quartz, with minor phengite, amphibole and rutile (Appendix B, Table B 2). The sample has a foliated microstructure defined by elongate matrix grains. Compositional banding is weakly developed but locally visible, with domains enriched in clinozoisite and kyanite (Figure 11a). Garnet occurs as coarse grains and commonly shows compositional variation in BSE contrast, with brighter domains along rims and withing the grain interior (Figure 11b). The zoning is less pronounced than in SZ-N-029. Chemical data show that garnet cores plot at relatively higher pyrope contents, whereas rims and parts of the interior are shifted toward relatively higher almandine contents and slightly higher grossular contents (Figure 10; Appendix B, Table B 4). Clinozoisite also shows zoning in several grains (Figure 11b). In contrast, no compositional zoning was observed in omphacite. Omphacite forms a major part of the matrix and occurs as elongate grains (Figure 11a,c). Grain boundaries between adjacent omphacite grains are generally straight. Small quartz grains occur locally at some triple junctions between omphacite grains (Figure 11d). No clear intracrystalline deformation features were observed in omphacite. Quartz occurs as coarse grains as well, and boundaries between quartz and omphacite are strongly lobate (Figure 11d,e). Symplectic intergrowths along grain boundaries are rare and less developed than in the sample SZ-N-029 (Figure 11d). Amphibole occurs along some garnet margins (Figure 11c), whereas rutile and phengite are present as minor phases.

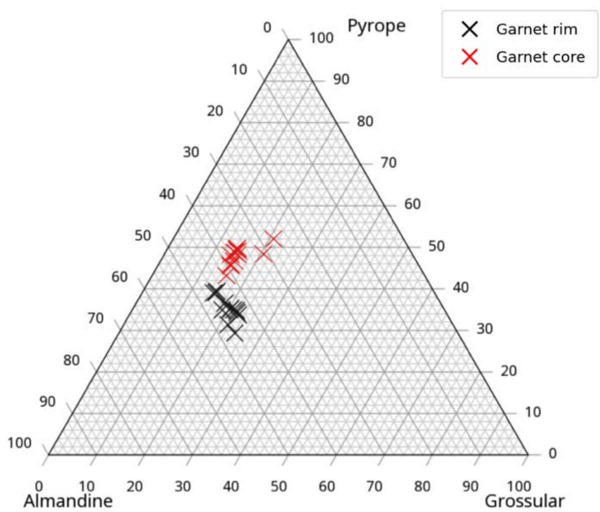


*Figure 10: Ternary diagram showing garnet compositions from sample SZ-N-059 plotted in the Alm-Prp-Grs system. Garnet cores plot at relatively higher pyrope contents, whereas garnet rims are shifted toward relatively higher almandine content and slightly higher grossular contents.*

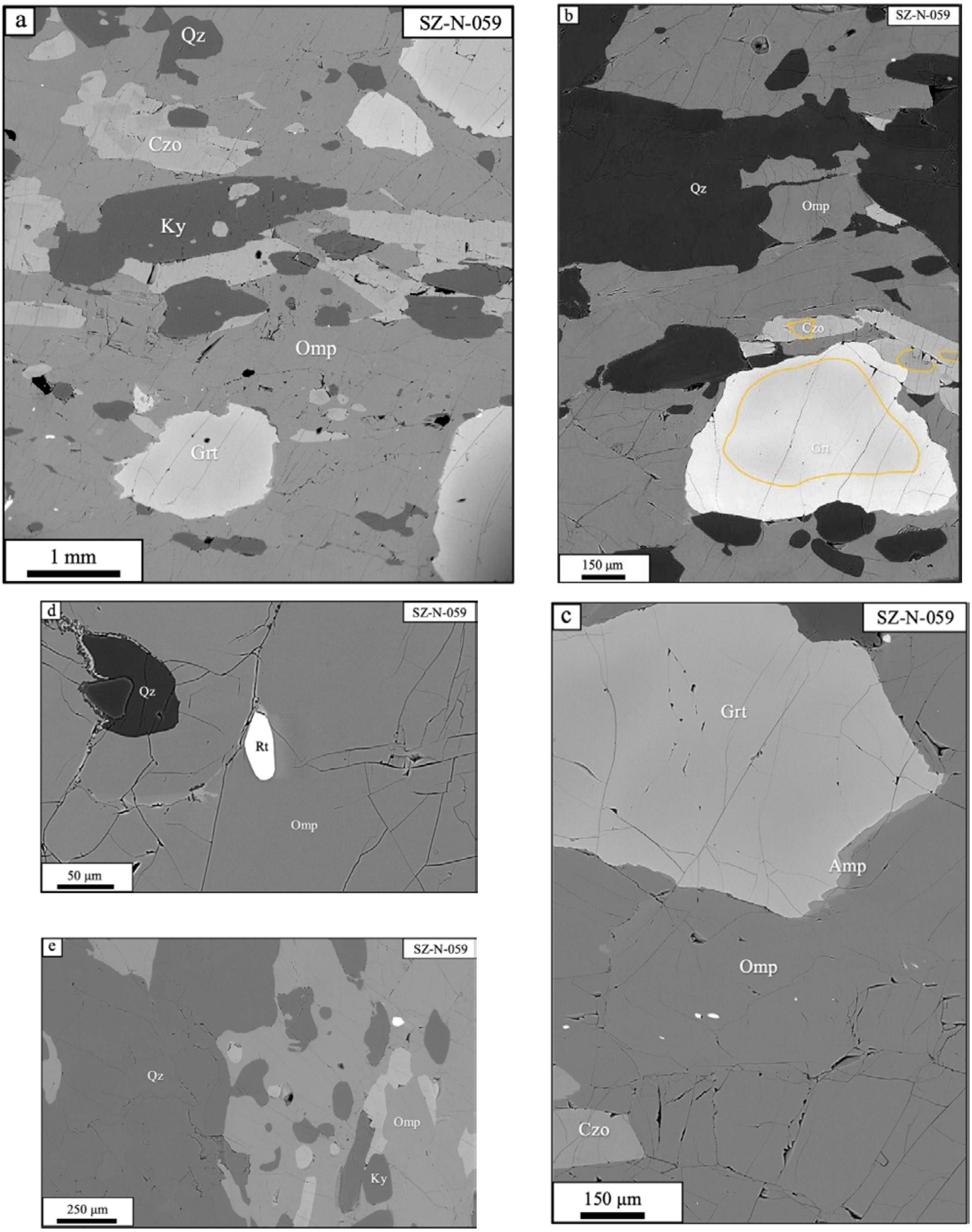


*Figure 11: BSE images of sample SZ-N-059. (a) Overview image showing weak compositional banding with a kyanite-clinozoisite rich domain, omphacite rich matrix, zoned clinozoisite and zoned garnet. (b) Domain containing quartz, omphacite, zoned clinozoisite and zoned garnet. (c) Omphacite rich matrix domain and amphibole along a garnet margin. (d) Rutile and symplectic intergrowths along a qz-omp grain boundary and small quartz grain at omphacite triple junction (e) Quartz grain with a lobate grain boundary against omphacite.*

## 5.3.Electron Backscatter Diffraction (EBSD)

EBSD analysis was carried out on sample SZ-N-059. In the EBSD output, clinopyroxene was indexed as diopside, white mica as muscovite and garnet as pyrope. Based on EDS and optical analysis, these phases are identified as omphacite, phengite and garnet.

The EBSD phase map shows that the mapped domain is dominated by omphacite (Figure 12a). Kyanite and garnet are also present, whereas quartz and clinozoisite are subordinate. Phengite and rutile occur in minor amounts. Garnet occurs as coarse grains within an omphacite rich matrix, whereas kyanite, quartz and clinozoisite occur as smaller grains and discontinuous bands. Most grain boundaries are high angle boundaries (>10°), whereas low angle boundaries (2-10°) are less common.

The inverse pole figure (IPF) map for omphacite, shown relative to the EBSD Z direction, shows elongate grains with variable crystallographic orientations across the mapped area (Figure 12b). Several neighbouring grains display similar orientations, while individual grains are generally internally uniform in orientation. Most grain boundaries are clearly defined and no widespread internal grain subdivision is visible. A few low angle boundaries are present in addition to the dominant high angle boundaries.

Omphacite pole figures show a crystallographic preferred orientation (CPO), expressed by clustering in the {100}, {010}, and {001} pole figures (Figure 12c). The strongest maximum occurs in the {010} pole figure, in the lower part of the plot toward Y1. The {100} pole figure shows several broader maxima across the upper half of the plot. The {001} pole figure also shows several maxima across the upper half and toward the right of the plot. The pole figures are plotted in the EBSD reference frame. The thin section was cut parallel to lineation and perpendicular to foliation, the EBSD X direction approximately corresponds to the structural lineation, whereas the EBSD Y direction corresponds approximately to the foliation normal. The grain reference orientation deviation (GROD) map for omphacite shows generally low internal misorientation across most of the mapped area (Figure 13a). Most omphacite grains display low GROD values, whereas only a few local domains show slightly elevated values up to ~10°. Isolated anomalous values associated with the holes in the sample or poorly indexed areas were excluded from interpretation. The grain orientation spread (GOS) map also shows that most omphacite grains display low grain orientation spread (Figure 13b). Values range up to ~4°, and most grains display low values. Together, GROD and GOS maps show that most omphacite grains have limited internal misorientation.

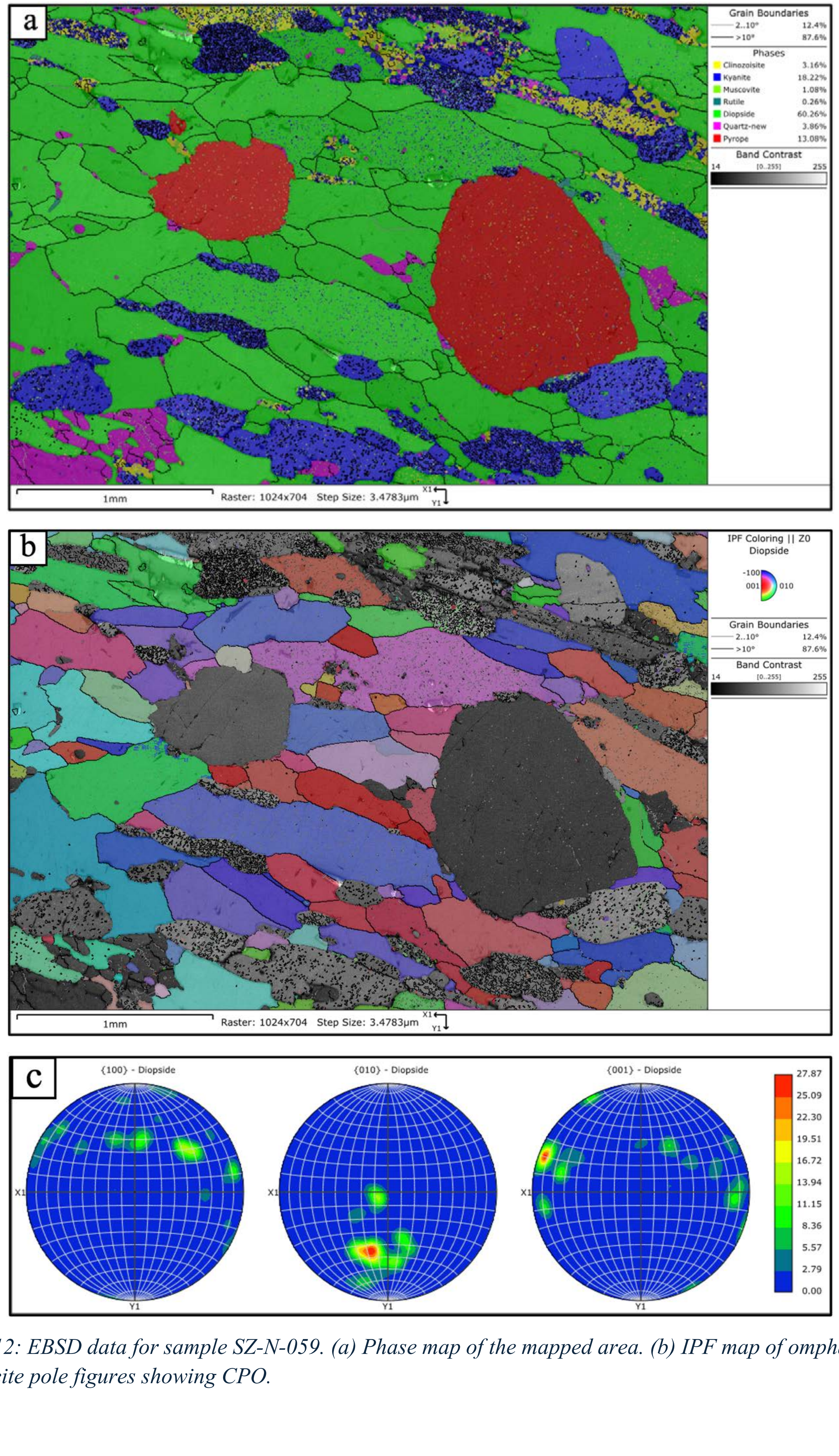


*Figure 12: EBSD data for sample SZ-N-059. (a) Phase map of the mapped area. (b) IPF map of omphacite. (c) Omphacite pole figures showing CPO.*

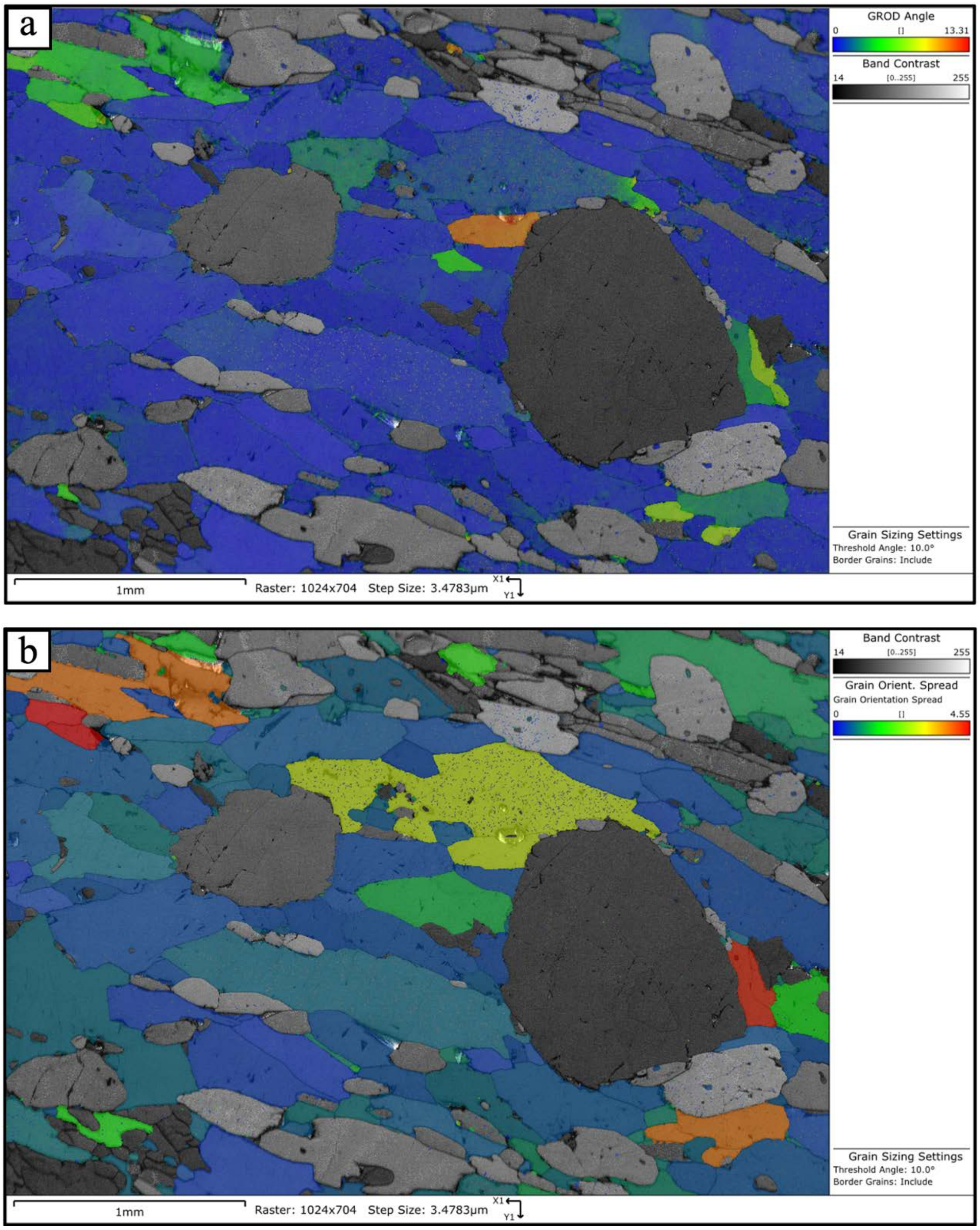


*Figure 13: EBSD data for sample SZ-N-059 (a) GROD map of omphacite. (b) GOS map of omphacite.*

*5.3.1 Additional EBSD observations*

Additional EBSD pole figures and GROD maps were generated for quartz, clinozoisite and kyanite in sample SZ-N-059. Quartz is included as supporting evidence because it was indexed sufficiently and quartz microstructures were observed by optical microscopy. Clinozoisite and kyanite are not used for detailed interpretation because their indexing quality was poor.

The quartz GROD map shows mostly low internal misorientation, with local areas of slightly elevated misorientation up to ~ 9° (Figure 14a). Grains are dominated by blue to green colours and the pattern occurring in individual grains is consistent with the observation of subgrains and undulose extinction. The quartz pole figures show a non random crystallographic orientation distribution, displaying a CPO (Figure 14b).

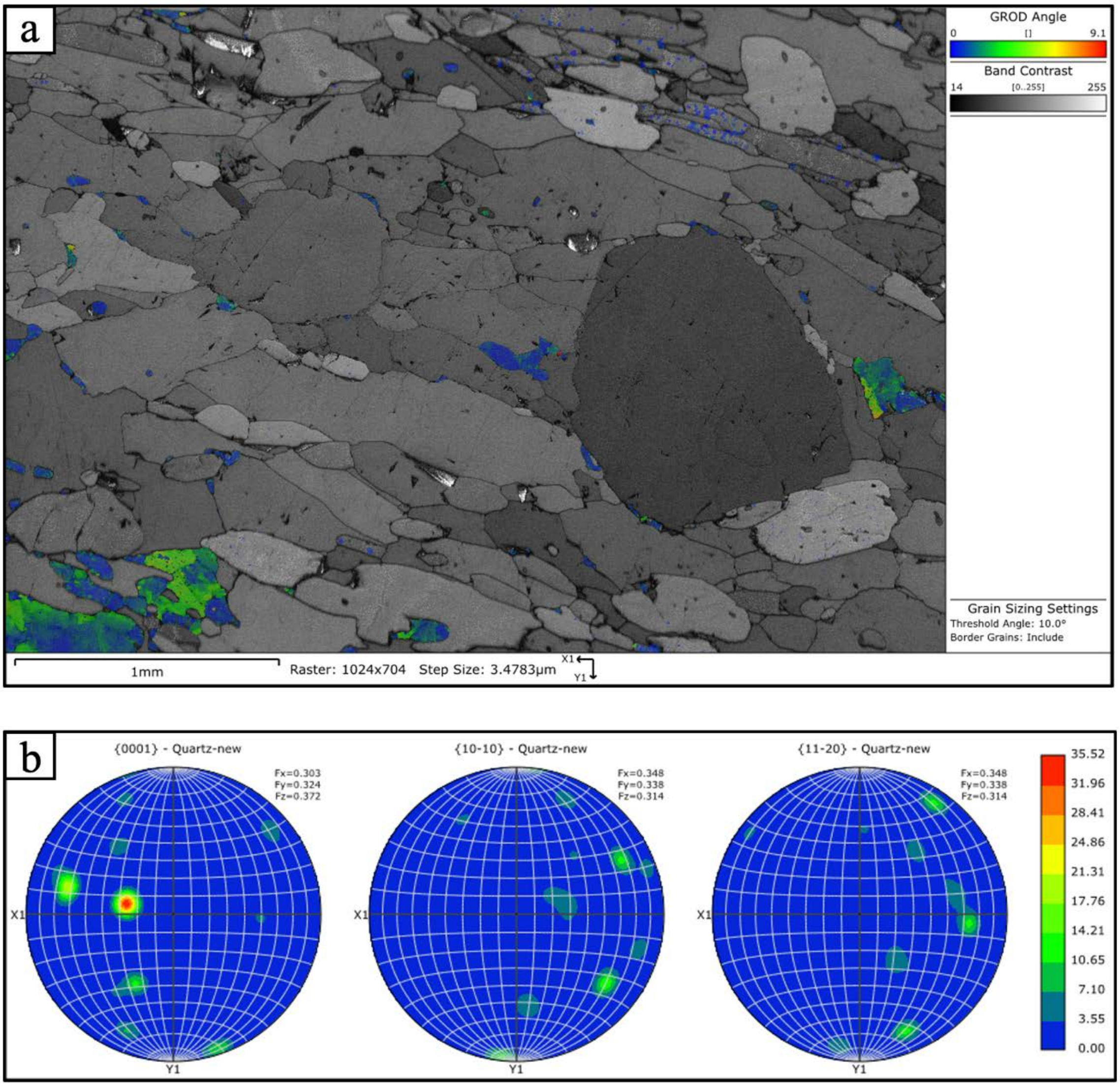


*Figure 14: EBSD data from sample SZ-N-059 showing GROD map and pole figures for quartz.*

# 6. Discussion

### 6.1 Microstructural context

The studied samples show variable fabric intensity. SZ-N-019 is characterized by coarse garnet grains and aggregates within a finer omphacite-rich matrix, whereas SZ-N-029 and SZ-N-059 show a more clearly developed foliation defined mainly by elongate omphacite grains and compositional banding. In SZ-N-059, the foliation is associated with omphacite-rich domains, quartz-bearing domains and kyanite-clinozoisite rich bands. This indicates that strain was not homogeneously distributed between all phases, but was partitioned into different mineralogical domains.

This interpretation is consistent with Bascou et al. (2001), who showed that omphacite commonly develops a stronger crystallographic fabric than garnet in deformed eclogites. Stünitz et al. (2020) showed that elongate omphacite grains can preserve strong CPO and very low internal misorientation, which they interpreted as preferential growth during diffusion creep. McNamara et al. (2024) described strong omphacite CPO with rare subgrain boundaries, weak undulose extinction and limited dislocation related microstructures, and interpreted the dominant process as diffusion mass transfer. Dutta et al. (2026) similarly interpreted elliptical, chemically unzoned omphacite grains with scarce subgrains as evidence for diffusion creep. The locally polygonal omphacite rich domains in SZ-N-019, with relatively straight grain boundaries and triple junctions approaching 120°, may reflect textural equilibration by grain boundary area reduction. Passchier and Trouw (2005) describe grain boundary area reduction as a process that reduces the internal free energy by straightening grain boundaries and producing polygonal grain shapes. Such microstructures may also develop during static recrystallization after deformation has slowed or stopped. Therefore, the polygonal domains in SZ-N-019 may reflect static recrystallization, but this interpretation remains cautious because the timing cannot be determined from optical observations alone. Grain boundary features are also important in SZ-N-059, where small quartz grains occur locally at some omphacite triple junctions. The microstructures are also consistent with deformation in a reacting and partly retrogressed system. Symplectic intergrowths occur locally along grain boundaries, amphibole is present along some garnet or omphacite margins, and garnet shows core-rim chemical differences. These features indicate that the studied rocks experienced mineral reactions and retrograde modification. This is important because Stünitz et al. (2020) and McNamara et al. (2024) showed that omphacite fabrics can form without dominant dislocation creep. Rogowitz and Huet (2021) further showed that eclogitization may involve dissolution-precipitation, transient porosity and weakening during fluid assisted transformation.

### 6.2 Omphacite as the main phase

Omphacite is the most important phase for interpreting deformation in the studied samples because it defines much of the foliation and forms the main matrix phase. In optical microscopy and SEM, omphacite commonly occurs as elongate grains aligned parallel to the foliation. EBSD data from SZ-N-059 also show that omphacite has a CPO. This means that the omphacite grains are not randomly oriented, but form an organized fabric. Bascou et al. (2001) found strong omphacite CPOs in eclogites and related them to dislocation glide on specific slip systems. Park and Jung (2019) similarly interpreted omphacite CPO together with subgrain boundaries and undulose extinction as evidence for intracrystalline deformation by dislocation creep. However, omphacite CPO is not unique to dislocation creep. Stünitz et al. (2020) showed that omphacite can develop strong CPO and SPO during diffusion creep, because omphacite grains may grow, dissolve or become redistributed in a preferred orientation during deformation without requiring dominant intracrystalline dislocation. McNamara et al. (2024) also argued that strong omphacite CPO can be produced where diffusion mass transfer processes are important. Dutta et al. (2026) provide a further comparison from Tso Morari eclogite, where elliptical omphacite grains with scarce subgrains and no chemical zoning were interpreted as having deformed by diffusion creep. Therefore, the omphacite CPO in SZ-N-059 does not by itself identify the deformation mechanism.

### 6.3 Dislocation creep interpretation

Dislocation creep involves intracrystalline plastic deformation by movement of dislocations through the crystal lattice. Microstructural evidence for dislocation creep commonly includes undulose extinction, subgrain boundaries, low angle boundaries, lattice bending, internal misorientation and dynamic recrystallization (Vernon, 2004; Passchier and Trouw, 2005). The studied samples contain some evidence that could be compatible with dislocation creep. Omphacite is elongate and defines a SPO, and the EBSD pole figures from SZ-N-059 show CPO. These observations are similar to ones described by Bascou et al. (2001), where omphacite CPO was interpreted in relation to dislocation glide. Therefore, a contribution from dislocation creep cannot be excluded. However, several observations argue against dominant dislocation creep in the studied omphacite. First, omphacite grains are generally internally uniform in optical microscopy and BSE images. Clear subgrain boundaries, strong undulose extinction and obvious dynamic recrystallization microstructures are not observed. Second, the EBSD data show generally low GROD and GOS values in omphacite. Third, low angle boundaries are rare compared with high angle boundaries. These observations indicate limited internal lattice distortion.

If dislocation creep had been the dominant mechanism, more widespread evidence of internal misorientation, subgrain development or lattice bending would be expected. The lack of these features weakens a dislocation creep interpretation, even though CPO is present. McNamara et al. (2024) reached a similar conclusion for omphacite with strong CPO, but rare subgrain boundaries and weak undulose extinction, which they interpreted as evidence for only limited dislocation creep. Stünitz et al. (2020) also showed that elongated omphacite grains can preserve strong CPO while remaining single crystals with little internal misorientation. Therefore, the combination of CPO and low internal misorientation in SZ-N-059 is not sufficient evidence for dominant dislocation creep.

Quartz in SZ-N-059 shows clearer undulose extinction and subgrain development than omphacite in optical microscopy. The EBSD data show local internal misorientation, although most indexed quartz domains also have relatively low GROD values. Therefore, quartz is interpreted to record local crystal plastic deformation and recovery, but the EBSD evidence should be treated as supporting evidence because not many quartz grains were present in the mapped area. The contrast with omphacite remains useful, because omphacite lacks clear optical evidence for subgrain development or strong undulose extinction.

### 6.4 Evidence for diffusion assisted and dissolution-precipitation assisted creep

The microstructural evidence is more consistent with diffusion assisted or dissolution-precipitation assisted deformation than with dominant dislocation creep. Diffusion creep and dissolution-precipitation creep can produce strain by mass transfer along grain boundaries, interphase boundaries or through a fluid phase. These processes may produce shape fabrics and even crystallographic fabrics without generating strong internal lattice distortion in individual grains. Grain boundary sliding (GBS) may also have contributed to the deformation of the omphacite rich matrix. Diffusion creep is commonly accommodated by GBS, because material transfer by diffusion or dissolution-precipitation must be accompanied by relative movement between grains. This interpretation is consistent with Passchier and Trouw (2005), who noted that diffusion creep leaves few direct microstructural traces and that GBS is difficult to identify directly. They further explained that the presence of a preferred orientation cannot be used as evidence against GBS. In this study, the occurrence of small quartz grains at some omphacite triple junctions in SZ-N-059 is therefore interpreted as supporting evidence for GBS during diffusion assisted deformation. This interpretation is supported by studies of creep cavitation. Fusseis et al. (2009) showed that diffusion creep in a ductile shear zone can involve GBS together with dissolution and precipitation, producing grain boundary porosity. Menegon et al. (2015)

similarly interpreted isolated grains and pores as evidence for creep cavitation during diffusion creep accommodated by GBS. In the present samples, small quartz grains occurring at some omphacite triple junctions are consistent with diffusion assisted deformation involving GBS and mass transfer along grain boundaries.

The absence of strong internal misorientation in omphacite does not prove diffusion creep directly, but it is consistent with grain boundary or mass transfer processes rather than dominant dislocation creep (Vernon, 2004; Passchier and Trouw, 2005). Stünitz et al. (2020) provide a close analogue for this interpretation. They described eclogites in which omphacite shows elongate grain shapes and CPO, but individual grains preserve little internal misorientation. They interpreted these fabrics as products of preferential crystal growth during diffusion creep, where metastable mafic phases dissolved and new eclogite-facies minerals precipitated. Their conclusion is relevant here because the studied omphacite also combines SPO and CPO with low internal misorientation. Following the interpretation of Stünitz et al. (2020), the omphacite fabric in SZ-N-059 can be explained by growth modified deformation during diffusion creep, rather than by dominant intracrystalline plasticity. Rogowitz and Huet (2021) also argued that eclogite deformation may be dominated by dissolution-precipitation creep, even where omphacite SPO and CPO are present. They emphasized that CPO and SPO are often interpreted as evidence for dislocation creep, but that such an interpretation may be misleading in reacting eclogites. This is important for the present study because the samples contain reaction related and retrograde features, including symplectic intergrowths, amphibole and phase boundary irregularities. These textures show that the rock was affected by mineral reactions and later local retrogression, making diffusion assisted or dissolution-precipitation assisted deformation plausible. McNamara et al. (2024) found strong omphacite CPO but rare subgrain boundaries, weak undulose extinction and limited dislocation related microstructures. They interpreted the dominant process as diffusion mass transfer, possibly pressure solution or Coble creep. Dutta et al. (2026) reached a similar interpretation. In their study, omphacite grains were elliptical, chemically unzoned and showed scarce subgrain development, which they interpreted as evidence for body diffusion creep. This is relevant to the present study because the omphacite in SZ-N-059 also shows a clear SPO and CPO, but lacks strong evidence for intracrystalline deformation.

Unlike McNamara et al. (2024), who used chemical zoning in omphacite as evidence for diffusion mass transfer, no clear compositional zoning was observed in omphacite in this study. Therefore, the interference colour variation in some omphacite grains in SZ-N-059 is not used here as evidence for chemical zoning. The colour variation may instead reflect optical effects such as orientation, local thickness variation or polishing effects. Although chemical zoning in omphacite was not observed in this study, the combination of omphacite CPO, low GROD and GOS values, and lack of well developed subgrain boundaries is similar to the criteria used by McNamara et al. (2024) to argue against dominant dislocation creep. They proposed that limited dislocation creep may have occurred first, followed by dominant diffusion creep. This provides a useful comparison for the studied Holsnøy samples, where the available microstructural evidence is most consistent with diffusion assisted or dissolution-precipitation assisted deformation, rather than dominant dislocation creep.

**6.5 Strain partitioning and the role of other phases**

Although omphacite is the main focus, the other phases provide evidence on how deformation was partitioned through the rock. Garnet occurs as coarse grains in all samples and commonly appears less internally deformed than the surrounding matrix. In SZ-N-029, the foliation is locally deflected around garnet, suggesting that garnet behaved more rigidly than the surrounding matrix. This interpretation is consistent with Bascou et al. (2001), who showed that garnet commonly has weak or random CPO while omphacite develops a stronger fabric. Stünitz et al. (2020) also reported random garnet CPO despite elongate shapes, which they interpreted as growth related rather than dislocation creep related. Garnet should not, however, be treated only as a passive rigid object. In SZ-N-029 and SZ-N-059, garnet shows core-rim chemical differences, with cores and rims differing in pyrope and almandine content. Salimgaraeva et al. (2025) showed that garnet cores in Bergen Arcs eclogites can preserve relic granulite-facies compositions, whereas garnet rims record chemical modification during eclogite-facies metamorphism. Hess et al. (2025) further showed that Holsnøy garnet rims may form through fluid assisted dissolution-reprecipitation reactions and may record episodic fluid infiltration. In SZ-N-059, garnet zoning is not limited to a simple core-rim pattern, because brighter BSE domains also occur locally within the grain interior. This suggests that heterogeneous chemical modification may have occurred along rims, fractures or internal reaction pathways. Raimbourg et al. (2007) described similar garnet re-equilibration on Holsnøy, where granulitic garnet was modified along rims and fractures during eclogite-facies metamorphism. The garnet zoning observed in this study is therefore consistent with incomplete replacement or modification during eclogitization.

Quartz records a different deformation behaviour. In SZ-N-059, quartz shows undulose extinction and subgrains in optical microscopy, suggesting local intracrystalline deformation and recovery. The quartz GROD map shows local internal misorientation, but the EBSD evidence is not strong enough to prove widespread quartz dislocation creep. These features are typical of intracrystalline deformation and recovery in quartz (Passchier and Trouw, 2005). The difference between quartz and omphacite suggests that, under the same conditions, different minerals accommodated deformation by different mechanisms. Quartz records crystal-plastic strain, whereas omphacite mainly records a shape and crystallographic fabric with limited internal distortion. This contrast supports deformation partitioning between mineral phases, rather than a single deformation mechanism operating uniformly throughout the rock. Dutta et al. (2026) also provide a useful example of phase dependent deformation in eclogite. They interpreted omphacite as deforming by body diffusion creep, whereas different symplectite minerals recorded either dislocation creep of diffusion creep depending on local fluid availability. This supports the interpretation that the Holsnøy samples should not be described by a single deformation mechanism acting equally in all phases.

Clinozoisite, kyanite, phengite, amphibole and symplectic intergrowths provide further evidence for reaction assisted deformation and retrograde modification. Clinozoisite and kyanite occur in compositional bands, indicating mineralogical differentiation during eclogite-facies recrystallization. Phengite is a hydrous phase and indicates the involvement of aqueous fluid, which is consistent with the interpretation of eclogitization on Holsnøy by Austrheim (1987). Symplectic intergrowths are interpreted as retrograde reaction features. Zertani et al. (2024) described that omphacite breakdown to symplectites is commonly linked to decompression and retrogression of eclogites. This is also consistent with Anderson and Moecher (2007), who interpreted symplectites as retrograde products formed during decompression from eclogite-facies conditions. Dutta et al. (2026) also showed that symplectites can replace omphacite during retrogression. In the present samples, these intergrowths are local and retrogression likely modified parts of the microstructure but did not completely overprint the eclogite-facies fabric.

### 6.6 Preferred deformation mechanism

The preferred interpretation is that studied eclogites record deformation during fluid assisted reaction, with omphacite fabric development dominated by diffusion assisted or dissolution-precipitation assisted processes and minor or local dislocation creep. This interpretation is based on five main observations.

First, omphacite forms the main matrix fabric and shows both SPO and CPO. This demonstrates that omphacite recorded deformation. Second, omphacite shows low GROD and GOS values, rare low angle boundaries and poorly developed subgrain or undulose extinction microstructures. This weakens the interpretation that the CPO formed mainly by dislocation creep. Third, quartz shows optical evidence for crystal-plastic deformation, including undulose extinction and subgrain development, whereas comparable evidence is absent in omphacite. Fourth, garnet zoning, compositional banding, irregular phase boundaries and the presence of hydrous phases indicate that deformation occurred in a reacting, fluid influenced rock. The presence of fluids and ongoing metamorphic reactions makes diffusion assisted, or dissolution-precipitation assisted deformation geologically plausible. Fifth, small quartz grains occur locally at some omphacite triple junctions. These grains are consistent with GBS and mass transfer along grain boundaries during diffusion assisted deformation.

This model is consistent with the broader evolution of Holsnøy. Jamtveit et al. (1990) showed that eclogitization in the Bergen Arcs was strongly controlled by fluid infiltration. Zertani et al. (2019) showed that eclogitization on Holsnøy occurred both dynamically in shear zones and statically in less deformed domains. Kaatz et al. (2021) showed that continued fluid supply can promote widening of hydrous eclogite-facies shear zones during progressive deformation. In this context, omphacite fabric is consistent with the regional model of reaction controlled transformation of dry lower crust. The studied samples therefore support a deformation model in which omphacite CPO does not automatically indicate dislocation creep. Instead, the microstructures suggest that omphacite fabric developed during a reaction assisted deformation process. This is similar to the interpretation of Stünitz et al. (2020), who linked eclogite fabric development to preferential growth during diffusion creep, and to McNamara et al. (2024), who argued that diffusion creep can dominate omphacite deformation even where CPO is strong. Dutta et al. (2026) further support this interpretation by showing that omphacite with scarce subgrains and no chemical zoning may record diffusion creep rather than dominant dislocation creep. The interpretation that diffusion assisted deformation may have been accompanied by GBS is also consistent with Fusseis et al. (2009), who linked diffusion creep to GBS, dissolution-precipitation and grain boundary porosity, and with Menegon et al. (2015), who interpreted isolated grains and pores as evidence for creep cavitation during diffusion creep accommodated by GBS.

The most cautious conclusion is that dislocation creep may have contributed locally or during an earlier stage, but the dominant omphacite deformation mechanism is diffusion creep.

### 6.7 Limitations and further work

This study was limited by the number of samples analysed with SEM and EBSD and by the amount of time available for analytical work. Eleven thin sections were examined at first, and three were chosen for detailed investigation by optical microscopy, two were analysed by SEM and one sample was analysed by EBSD. The EBSD interpretation represents one mapped area from one sample and cannot be assumed to represent all samples equally. The EBSD data quality also limits the interpretation. Omphacite was the most reliably indexed phase, whereas quartz, kyanite and clinozoisite were less consistently indexed. Another limitation is that SEM and EBSD were new methods in this project, and considerable time was required to learn the instrument controls, acquisition procedure and processing software. If the study were repeated, more time would be spent on selecting EBSD areas after detailed SEM screening, especially in well polished, omphacite rich domains.

# 7. Conclusion

This study characterized deformation microstructures in eclogites from Holsnøy, western Norway, using optical microscopy and SEM including EBSD. The studied samples contain garnet and omphacite rich eclogite-facies assemblages with variable foliation intensity, compositional banding, local reaction textures and retrograde modification. Omphacite is the main fabric forming phase in the studied samples. In SZ-N-029 and SZ-N-059, elongate omphacite grains define the foliation and EBSD data show that omphacite has a CPO. However, the omphacite grains generally show low internal misorientation, low GROD and GOS values, and limited evidence for subgrain development. These observations do not support dominant dislocation creep as the main deformation mechanism. Instead, the omphacite microstructures are more consistent with deformation by diffusion assisted or dissolution-precipitation assisted processes, probably accompanied by GBS and mass transfer along grain boundaries. A minor or local contribution from dislocation creep cannot be excluded, but the available optical, SEM and EBSD data suggest that it was not the dominant mechanism. The results therefore show that omphacite CPO alone should not be interpreted as direct evidence for dislocation creep. In eclogites such as those from Holsnøy, omphacite SPO and CPO may also form during diffusion assisted mineral growth and mass transfer. This highlights the importance of combining CPO data with optical, SEM and EBSD microstructural observations when interpreting deformation mechanisms in eclogites.

## 8. Acknowledgements

I would like to thank my supervisor, Sascha Zertani, for his guidance, feedback and support throughout this project. I am also grateful to Andreas Karlsson at the Swedish Museum of Natural History for his assistance with SEM and EBSD work. I would especially like to thank my partner and my family for their constant encouragement, patience and support throughout my studies. Finally, I thank my friends for their support during the preparation of this thesis.

## 9. References


Anderson, Eric D. & Moecher, David P. (2007). Omphacite breakdown reactions and relation to eclogite exhumation rates. *Contributions to Mineralogy and Petrology*, 154, p. 253–277. doi: https://doi.org/10.1007/s00410-007-0192-x

Austrheim, Håkon. (1987). Eclogitization of lower crustal granulites by fluid migration through shear zones. *Earth and Planetary Science Letters*, 81, p. 221–232.

Bascou, Jérôme., Barruol, Guilhem., Vauchez, Alain., Mainprice, David. & Egydio-Silva, Marcos. (2001). EBSD-measured lattice-preferred orientations and seismic properties of eclogites. *Tectonophysics*, 342(1–2), p. 61–80. doi: https://doi.org/10.1016/S0040-1951(01)00156-1

Bhowany, Kishan., Hand, Martin., Clark, Chris., Kelsey, David E., Reddy, Steven M., Pearce, Mark A., Tucker, Nicholas M. & Morrissey, Liam J. (2018). Phase equilibria modelling constraints on P–T conditions during fluid catalysed conversion of granulite to eclogite in the Bergen Arcs, Norway. *Journal of Metamorphic Geology*, 36(3), p. 315–342. doi: https://doi.org/10.1111/jmg.12294

Dutta, Dripta., Imayama, Takeshi., Sarkar, Dyuti Prakash., Ando, Jun-ichi. & Das, Kaushik. (2026). Creep behaviour of omphacite and amphibole-plagioclase symplectite: the role of heterogeneous hydration in the Tso Morari eclogite during retrogression. *Contributions to Mineralogy and Petrology*, 181, 1. doi: https://doi.org/10.1007/s00410-025-02281-x

Fusseis, Florian., Regenauer-Lieb, Klaus., Liu, Jianfeng., Hough, Robert M. & De Carlo, Francesco. (2009). Creep cavitation can establish a dynamic granular fluid pump in ductile shear zones. *Nature*, 459, p. 974–977. doi: https://doi.org/10.1038/nature08051

Hess, Benjamin L., Ague, Jay J. & Austrheim, Håkon. (2025). Coupled diffusion and stress in garnet from Holsnøy, Norway: implications for mineral replacement reactions and the timescales of episodic heating and fluid flow during subduction. *Journal of Petrology*, 66(10), egaf083. doi: https://doi.org/10.1093/petrology/egaf083

Jamtveit, Bjørn., Bucher-Nurminen, Katrin. & Austrheim, Håkon. (1990). Fluid controlled eclogitization of granulites in deep crustal shear zones, Bergen Arcs, Western Norway. *Contributions to Mineralogy and Petrology*, 104(2), p. 184–193. doi: https://doi.org/10.1007/BF00306442

Kaatz, Lisa., Zertani, Sascha., Moulas, Evangelos., John, Timm., Labrousse, Loïc., Schmalholz, Stefan M. & Andersen, Torgeir B. (2021). Widening of hydrous shear zones during incipient eclogitization of metastable dry and rigid lower crust—Holsnøy, western Norway. *Tectonics*, 40, e2020TC006572. doi: https://doi.org/10.1029/2020TC006572

McNamara, David D., Wheeler, John., Pearce, Mark A. & Prior, David J. (2024). A key role for diffusion creep in eclogites: Omphacite deformation in the Zermatt-Saas unit, Italian Alps. *Journal of Structural Geology*, 179, 105033. doi: https://doi.org/10.1016/j.jsg.2023.105033

Menegon, Luca., Fusseis, Florian., Stünitz, Holger. & Xiao, Xianghui. (2015). Creep cavitation bands control porosity and fluid flow in lower crustal shear zones. *Geology*, 43(3), p. 227–230. doi: https://doi.org/10.1130/G36307.1

Park, Minsu. & Jung, Haemyeong. (2019). Relationships between eclogite-facies mineral assemblages, deformation microstructures, and seismic properties in the Yuka Terrane, North Qaidam ultrahigh-pressure metamorphic belt, NW China. *Journal of Geophysical Research: Solid Earth*, 124(12), p. 13168–13191. doi: https://doi.org/10.1029/2019JB018198

Passchier, Cees W. & Trouw, Rudolph A. J. (2005). *Microtectonics*. 2nd ed. Berlin: Springer.

Raimbourg, Hugues., Goffé, Bruno. & Jolivet, Laurent. (2007). Garnet reequilibration and growth in the eclogite facies and geodynamical evolution near peak metamorphic conditions. *Contributions to Mineralogy and Petrology*, 153, p. 1–28. doi: https://doi.org/10.1007/s00410-006-0130-3

Rogowitz, Anna. & Huet, Benjamin. (2021). Evolution of fluid pathways during eclogitization and their impact on formation and deformation of eclogite: A microstructural and petrological investigation at the type locality, Koralpe, Eastern Alps, Austria. *Tectonophysics*, 819, 229079. doi: https://doi.org/10.1016/j.tecto.2021.229079

Salimgaraeva, Laysan I., Skublov, Sergey G., Berezin, Aleksey V. & Galankina, Olga L. (2025). Granulite-to-eclogite conversion at the Bergen Arcs, South Norway, as recorded in garnet and zircon zoning. *Lithos*, 518–519, 108329. doi: https://doi.org/10.1016/j.lithos.2025.108329

Stünitz, Holger., Neufeld, Kristina., Heilbronner, Renée., Finstad, Ane K., Konopásek, Jiří. & Mackenzie, James R. (2020). Transformation weakening: Diffusion creep in eclogites as a result of interaction of mineral reactions and deformation. *Journal of Structural Geology*, 139, 104129. doi: https://doi.org/10.1016/j.jsg.2020.104129

Vernon, Ronald H. (2004). *A Practical Guide to Rock Microstructure*. Cambridge: Cambridge University Press.

Zertani, Sascha., Labrousse, Loïc., John, Timm., Andersen, Torgeir B. & Tilmann, Frederik. (2019). The interplay of eclogitization and deformation during deep burial of the lower continental crust—A case study from the Bergen Arcs, western Norway. *Tectonics*, 38(3), p. 898–915. doi: https://doi.org/10.1029/2018TC005297

Zertani, Sascha., John, Timm., Brachmann, Christoph., Vrijmoed, Johannes C. & Plümper, Oliver. (2022). Reactive fluid flow guided by grain-scale equilibrium reactions during eclogitization of dry crustal rocks. *Contributions to Mineralogy and Petrology*, 177, 61. doi: https://doi.org/10.1007/s00410-022-01928-3

Zertani, Sascha., Morales, Luiz F. G. & Menegon, Luca. (2024). Omphacite breakdown: nucleation and deformation of clinopyroxene–plagioclase symplectites. *Contributions to Mineralogy and Petrology*, 179, 44. doi: https://doi.org/10.1007/s00410-024-02125-0

# 10. Appendix

## 10.1 A - Grain size measurements

*Table A 1: Grain size measurements for sample SZ-N-019*

| SZ-N-019 | Omp Coarse (mm) | Omp Fine (mm) | Garnet (mm) |
|---|---|---|---|
| 1 | 0,87 | 0,33 | 2,31 |
| 2 | 0,62 | 0,21 | 0,84 |
| 3 | 1,37 | 0,23 | 0,81 |
| 4 | 0,79 | 0,16 | 0,44 |
| 5 | 0,48 | 0,09 | 0,23 |
| 6 | 0,54 | 0,10 | 0,75 |
| 7 | 0,53 | 0,06 | 0,82 |
| 8 | 0,42 | 0,12 | 0,51 |
| 9 | 0,84 | 0,07 | 0,54 |
| 10 | 0,63 | 0,09 | 1,98 |
| 11 | 0,87 | 0,14 | 0,32 |
| 12 | 0,75 | 0,17 | 0,73 |
| 13 | 1,94 | 0,21 | 0,21 |
| 14 | 1,46 | 0,09 | 0,47 |
| 15 | 0,60 | 0,04 | 0,32 |
| 16 | 0,60 | 0,13 | 0,17 |
| 17 | 0,40 | 0,14 | 0,26 |
| 18 | 0,51 | 0,30 | 4,90 |
| 19 | 0,82 | 0,07 | 1,78 |
| **Median** | 0,63 | 0,13 | 0,54 |
| **AVG** | 0,79 | 0,14 | 0,97 |

*Table A 2: Grain size measurements for sample SZ-N-029*

| SZ-N-029 | Omphacite (mm) | Kyanite (mm) | Garnet (mm) |
|---|---|---|---|
| 1 | 0,82 | 0,16 | 1,01 |
| 2 | 1,10 | 0,11 | 0,87 |
| 3 | 0,91 | 0,23 | 1,67 |
| 4 | 0,64 | 0,14 | 2,03 |
| 5 | 2,71 | 0,10 | 2,22 |
| 6 | 0,49 | 0,03 | 1,84 |
| 7 | 0,63 | 0,06 | 1,15 |
| 8 | 1,05 | 0,08 | 2,66 |
| 9 | 1,20 | 0,04 | 1,06 |
| 10 | 0,49 | 0,09 | |
| 11 | 1,19 | 0,06 | |
| 12 | 1,36 | 0,15 | |
| 13 | 0,83 | 0,14 | |
| 14 | 1,25 | 0,10 | |
| 15 | 0,55 | 0,22 | |
| 16 | 0,63 | 0,25 | |
| 17 | 2,14 | 0,08 | |
| 18 | 1,74 | 0,19 | |
| 19 | 1,40 | 0,14 | |
| 20 | 0,44 | 0,23 | |
| 21 | 0,62 | 0,04 | |
| **Median** | 0,91 | 0,11 | 1,67 |
| **AVG** | 1,06 | 0,13 | 1,61 |

*Table A 3: Grain size measurements for sample SZ-N-059*

| SZ-N-059 | Omphacite (mm) | Kyanite (mm) | Garnet (mm) | Quartz (mm) |
|---|---|---|---|---|
| 1 | 0,75 | 0,18 | 1,85 | 1,98 |
| 2 | 0,81 | 0,18 | 2,04 | 1,25 |
| 3 | 0,41 | 0,22 | 0,65 | 1,21 |
| 4 | 0,56 | 0,10 | 1,05 | 2,58 |
| 5 | 1,45 | 0,12 | 1,25 | 1,28 |
| 6 | 0,69 | 0,05 | 1,77 | 0,58 |
| 7 | 0,72 | 0,10 | 1,18 | 0,84 |
| 8 | 0,98 | 1,08 | 0,69 | 0,71 |
| 9 | 0,58 | 0,06 | 0,92 | 0,59 |
| 10 | 0,44 | 0,14 | 1,25 | 0,42 |
| 11 | 0,25 | 0,06 | 1,27 | |
| 12 | 0,96 | 0,10 | 0,79 | |
| 13 | 0,64 | 0,27 | 0,92 | |
| 14 | 0,63 | 0,13 | 1,06 | |
| 15 | 1,51 | 0,11 | 1,33 | |
| 16 | 1,49 | 0,33 | 2,01 | |
| 17 | 0,30 | 0,12 | 1,35 | |
| 18 | 0,43 | 0,15 | 0,89 | |
| 19 | 0,86 | 0,13 | 1,24 | |
| 20 | 1,40 | 0,10 | 1,35 | |
| 21 | 1,38 | 0,02 | | |
| 22 | 0,93 | 0,12 | | |
| 23 | 0,76 | 0,28 | | |
| 24 | 0,90 | 0,18 | | |
| **Median** | 0,76 | 0,13 | 1,25 | 1,03 |
| **AVG** | 0,83 | 0,18 | 1,24 | 1,14 |

## 10.2 B - SEM phase chemistry

*Table B 1: SEM phase chemistry for sample SZ-N-029*

| Omphacite | Na2O | MgO | Al2O3 | SiO2 | CaO | MnO | FeO | Total |
|---|---|---|---|---|---|---|---|---|
| Spectrum 4 | 5,83 | 5,66 | 10,85 | 45,23 | 10,41 | | 4,54 | 82,52 |
| Spectrum 9 | 5,91 | 6,67 | 10,94 | 48,2 | 11,79 | | 4,36 | 87,87 |
| Spectrum 19 | 6,72 | 6,36 | 12,75 | 51,07 | 11,46 | | 5,08 | 93,43 |
| Spectrum 23 | 6,63 | 6,73 | 12,7 | 52,52 | 12,13 | | 5,16 | 95,88 |
| Spectrum 31 | 6,5 | 7,21 | 12,91 | 53,73 | 12,78 | | 5,2 | 98,33 |
| Spectrum 32 | 6,42 | 7,08 | 12,64 | 50,49 | 12,39 | | 5,1 | 94,12 |
| Spectrum 63 | 6,23 | 6,16 | 11,78 | 48,85 | 11,28 | | 4,44 | 88,74 |
| Spectrum 64 | 6,43 | 6,09 | 12,31 | 49,49 | 11,02 | | 4,3 | 89,65 |
| Spectrum 65 | 7,12 | 7 | 13,22 | 55,04 | 12,39 | | 4,91 | 99,69 |
| Spectrum 66 | 6,83 | 6,55 | 13,11 | 52,62 | 11,7 | | 4,85 | 95,66 |
| Spectrum 68 | 6,81 | 6,78 | 13,25 | 54,1 | 12,22 | | 4,76 | 97,93 |
| Spectrum 75 | 6,36 | 5,78 | 12,19 | 48,52 | 10,73 | | 4,29 | 87,87 |
| Spectrum 76 | 5,77 | 5,69 | 11,38 | 46,09 | 10,56 | | 4,12 | 83,61 |
| Spectrum 77 | 5,82 | 5,81 | 10,89 | 44,95 | 10,42 | | 4,06 | 81,96 |
| Spectrum 78 | 6,87 | 6,42 | 12,78 | 51,45 | 11,76 | | 4,49 | 93,78 |
| Spectrum 85 | 7,07 | 6,9 | 13,87 | 55,38 | 12,55 | | 5,08 | 100,84 |
| Spectrum 89 | 6,03 | 7,04 | 11,63 | 49,87 | 12,4 | | 4,63 | 91,81 |
| Spectrum 90 | 6,43 | 6,71 | 12 | 51,17 | 11,69 | | 4,21 | 92,21 |
| Spectrum 91 | 6,58 | 6,96 | 12,8 | 52,86 | 12,4 | | 4,54 | 96,14 |
| Spectrum 92 | 6,02 | 6,29 | 11,29 | 48,2 | 11,32 | | 4,04 | 87,17 |
| Spectrum 95 | 6,17 | 6,71 | 11,95 | 50,07 | 11,58 | | 4,34 | 90,82 |
| Spectrum 96 | 6,03 | 6,1 | 11,51 | 47,83 | 11,07 | | 4,21 | 86,75 |

| Kyanite | Na2O | MgO | Al2O3 | SiO2 | CaO | MnO | FeO | Total | |
|---|---|---|---|---|---|---|---|---|---|
| Spectrum 3 | | | 60 | 34,47 | | | 0,52 | 95 | |
| Spectrum 8 | | | 59,43 | 33,7 | | | 0,56 | 93,69 | |
| Spectrum 17 | | | 59,86 | 33,45 | | | 0,47 | 93,78 | |
| Spectrum 25 | | | 60,81 | 34,93 | | | 0,5 | 96,24 | |
| Spectrum 34 | | | 58,06 | 33,01 | | | 0,54 | 91,61 | |
| Spectrum 67 | | | 62,82 | 35,66 | | | 0,47 | 98,94 | |
| Spectrum 86 | | | 64,34 | 36,35 | | | 0,46 | 101,16 | |
| Spectrum 87 | | | 60,72 | 34,33 | | | 0,48 | 95,53 | |
| Spectrum 94 | | | 57,78 | 33 | | | 0,49 | 91,27 | |
| **Clinozoisite** | **Na2O** | **MgO** | **Al2O3** | **SiO2** | **CaO** | **MnO** | **FeO** | **WO3** | **Total** |
| Spectrum 7 | | | 32,79 | 39,18 | 24,99 | | 2,53 | -0,17 | 99,32 |
| Spectrum 10 | | | 28,25 | 33,58 | 21,63 | | 2,08 | 0,16 | 85,7 |
| Spectrum 15 | | | 30,28 | 36,72 | 23,21 | | 2,51 | | 92,72 |
| Spectrum 33 | | | 30,12 | 36,44 | 22,95 | | 2,41 | | 91,92 |
| Spectrum 69 | | | 28,35 | 33,73 | 21,7 | | 2,12 | -0,4 | 85,5 |
| Spectrum 71 | | | 29,89 | 36,35 | 23,21 | | 2,11 | | 91,56 |
| Spectrum 88 | | | 31,69 | 38,54 | 24,42 | | 2,51 | | 97,16 |
| **Phengite** | **Na2O** | **MgO** | **Al2O3** | **SiO2** | **K2O** | **TiO2** | **FeO** | **BaO** | **Total** |
| Spectrum 16 | 1,55 | 1,99 | 30,05 | 43,46 | 8,34 | 0,36 | 1,42 | 0,85 | 88,01 |
| Spectrum 18 | 1,54 | 2,02 | 29,83 | 43,54 | 8,03 | 0,44 | 1,67 | 0,93 | 87,99 |
| Spectrum 24 | 1,58 | 2,2 | 30,66 | 45,21 | 8,37 | 0,31 | 1,8 | 1,06 | 91,2 |
| Spectrum 27 | 1,69 | 1,77 | 28,49 | 40,86 | 7,29 | 0,33 | 1,54 | 0,83 | 82,8 |
| Spectrum 70 | 1,59 | 2,29 | 32,52 | 47,62 | 9,2 | 0,27 | 1,79 | 0,99 | 96,28 |

| Spectrum 72 | 1,59 | 2,08 | 30,81 | 44,77 | 8,43 | 0,45 | 1,55 | 0,88 | 90,57 |
|---|---|---|---|---|---|---|---|---|---|
| Spectrum 73 | 1,73 | 2,14 | 31,82 | 46 | 8,5 | 0,27 | 1,58 | 1,18 | 93,22 |
| Spectrum 74 | 1,62 | 2,08 | 31,09 | 45,19 | 8,55 | 0,34 | 1,66 | 1,04 | 91,58 |
| Spectrum 79 | 1,58 | 2 | 31,23 | 45,04 | 8,52 | 0,42 | 1,48 | 0,88 | 91,16 |
| Spectrum 80 | 1,5 | 2,09 | 32 | 46,43 | 8,95 | 0,42 | 1,32 | 0,95 | 93,67 |
| Spectrum 93 | 1,69 | 1,83 | 28,83 | 41,92 | 7,63 | 0,47 | 1,43 | 0,84 | 84,64 |
| **Amphibole** | **Na2O** | **MgO** | **Al2O3** | **SiO2** | **K2O** | **CaO** | **TiO2** | **FeO** | **Total** |
| Spectrum 28 | 4,04 | 10,69 | 17,45 | 41,21 | 0,89 | 9,97 | 0,33 | 13,5 | 98,09 |
| Spectrum 35 | 4,35 | 10,22 | 17,13 | 39,03 | 0,79 | 8,09 | 0,24 | 10,69 | 90,54 |
| **Garnet Rim** | **Na2O** | **MgO** | **Al2O3** | **SiO2** | **CaO** | **MnO** | **FeO** | **WO3** | **Total** |
| Spectrum 5 | | 8,02 | 21,75 | 37,23 | 7,65 | 0,95 | 24,38 | | 99,99 |
| Spectrum 12 | | 9,06 | 21,78 | 37,26 | 6,71 | 0,63 | 22,35 | 0,18 | 97,98 |
| Spectrum 21 | | 8,1 | 22,05 | 38,46 | 7,87 | 0,81 | 23,44 | | 100,72 |
| Spectrum 29 | | 6,66 | 17,16 | 33,01 | 8,13 | 0,75 | 22,2 | | 89,36 |
| Spectrum 82 | | 7,23 | 21,71 | 37,65 | 8,71 | 0,87 | 22,45 | | 98,63 |
| Spectrum 84 | | 7,87 | 22,27 | 38,92 | 8,66 | 0,89 | 22,67 | | 101,29 |
| **Garnet Core** | **Na2O** | **MgO** | **Al2O3** | **SiO2** | **CaO** | **MnO** | **FeO** | **WO3** | **Total** |
| Spectrum 6 | | 13,7 | 20,79 | 36,41 | 6,99 | | 13,94 | | 91,83 |
| Spectrum 11 | | 13,76 | 21,87 | 38,05 | 7,56 | | 14,6 | | 95,84 |
| Spectrum 22 | | 14,75 | 23,47 | 40,68 | 7,99 | 0,23 | 14,13 | | 101,24 |
| Spectrum 30 | | 13,71 | 21,3 | 37,93 | 7,29 | | 14,75 | | 94,98 |
| Spectrum 81 | | 13,43 | 21,27 | 36,92 | 7,18 | 0,87 | 12,89 | | 98,63 |
| Spectrum 83 | | 14,62 | 23,03 | 40,47 | 7,68 | | 14,36 | | 100,16 |

*Table B 2: SEM phase chemistry for sample SZ-N-059*

| Omphacite | Na2O | MgO | Al2O3 | SiO2 | CaO | MnO | FeO | Total |
|---|---|---|---|---|---|---|---|---|
| Spectrum 1 | 5,46 | 7,54 | 11,4 | 49,93 | 13,1 | | 3,24 | 90,66 |
| Spectrum 10 | 3,7 | 11,82 | 16,7 | 42,29 | 9,29 | | 8,12 | 93,05 |
| Spectrum 13 | 6,27 | 8,4 | 12,58 | 55,32 | 14,02 | | 3,73 | 100,33 |
| Spectrum 38 | 5,76 | 8,22 | 11,54 | 53,73 | 13,95 | | 3,54 | 96,99 |
| Spectrum 39 | 6,07 | 7,99 | 11,94 | 53,11 | 13,52 | | 3,39 | 96,03 |
| Spectrum 69 | 5,89 | 7,75 | 11,5 | 50,88 | 13,53 | | 3,37 | 92,93 |
| Spectrum 72 | 5,94 | 8,37 | 11,95 | 54,35 | 14,08 | | 3,67 | 98,36 |
| Spectrum 73 | 5,65 | 8,03 | 11,18 | 51,43 | 13,4 | | 3,44 | 93,12 |
| Spectrum 74 | 5,89 | 8,08 | 12,03 | 50,87 | 13,71 | | 3,47 | 93,58 |
| Spectrum 75 | 5,41 | 7,6 | 10,95 | 49,76 | 13,1 | | 3,28 | 90,1 |
| Spectrum 76 | 5,42 | 8,01 | 10,81 | 50,64 | 13,63 | | 3,5 | 92,02 |
| Spectrum 78 | 6,04 | 8,55 | 12,66 | 54,77 | 14,18 | | 3,67 | 99,77 |
| Spectrum 82 | 5,98 | 8,53 | 11,57 | 54,32 | 14,27 | | 3,66 | 98,55 |
| Spectrum 83 | 5,72 | 8,2 | 11,62 | 52,84 | 13,9 | | 3,59 | 95,87 |
| Spectrum 84 | 5,6 | 7,44 | 11,63 | 50,75 | 13,05 | | 3,2 | 91,88 |
| Spectrum 93 | 5,59 | 8,29 | 12,13 | 53,51 | 14,37 | | 3,37 | 97,27 |
| Spectrum 99 | 5,74 | 8,17 | 11,93 | 52,42 | 13,84 | | 3,35 | 95,66 |
| Spectrum 100 | 5,28 | 8,57 | 11,15 | 52,37 | 15,19 | | 4,02 | 96,58 |
| Spectrum 101 | 6,04 | 8,27 | 12,31 | 53,25 | 13,84 | | 3,47 | 97,46 |
| Spectrum 106 | 5,97 | 8,07 | 12,27 | 53,57 | 14,24 | | 3,36 | 97,49 |
| Spectrum 107 | 5,36 | 7,32 | 10,86 | 47,24 | 12,19 | | 3,11 | 86,35 |
| Spectrum 108 | 5,49 | 7,69 | 10,86 | 49,66 | 13,08 | | 3,37 | 90,14 |

| | | | | | | | | |
|---|---|---|---|---|---|---|---|---|
| Spectrum 109 | 6,02 | 8,46 | 12,41 | 54,88 | 14,49 | | 3,56 | 100,05 |
| Spectrum 26 | 5,62 | 7,8 | 11,5 | 51,07 | 12,94 | | 3,38 | 92,51 |
| Spectrum 27 | 5,04 | 4,07 | 9,7 | 70,74 | 9,23 | | 1,55 | 100,35 |
| Spectrum 44 | 6,11 | 8,42 | 11,37 | 53,49 | 13,84 | | 4,02 | 97,26 |
| Spectrum 47 | 5,65 | 7,94 | 11,58 | 51,42 | 13,66 | | 3,57 | 93,91 |
| Spectrum 55 | 5,99 | 8,24 | 12,35 | 53,79 | 13,98 | | 3,9 | 98,49 |
| Spectrum 60 | 5,73 | 7,55 | 11,46 | 49,67 | 12,76 | | 3,55 | 90,72 |
| Spectrum 61 | 5,37 | 5,95 | 10,38 | 43,11 | 10,12 | | 3,04 | 78,18 |
| Spectrum 62 | 5,61 | 7,7 | 11,54 | 50,4 | 12,76 | | 3,5 | 91,5 |
| **Kyanite** | **Na2O** | **MgO** | **Al2O3** | **SiO2** | **CaO** | **MnO** | **FeO** | **Total** |
| Spectrum 5 | | | 48,79 | 27,86 | | | 0,32 | 76,97 |
| Spectrum 6 | | | 60,37 | 34 | | | 0,33 | 94,7 |
| Spectrum 7 | | | 57,79 | 32,67 | | | 0,27 | 90,73 |
| Spectrum 19 | | | 55,11 | 31,37 | | | 0,28 | 86,76 |
| Spectrum 21 | | | 57,89 | 32,25 | | | 0,32 | 90,47 |
| Spectrum 22 | | | 62,23 | 34,86 | | | 0,4 | 97,49 |
| Spectrum 24 | | | 61,11 | 34,64 | | | 0,28 | 96,03 |
| Spectrum 55 | | | 48,59 | 27,61 | | | 0,44 | 76,64 |
| Spectrum 61 | | | 53,92 | 30,58 | | | 0,28 | 84,78 |
| Spectrum 79 | | | 63,23 | 35,45 | | | 0,56 | 99,25 |
| Spectrum 46 | | | 61,03 | 34,71 | | | 0,34 | 96,07 |
| Spectrum 49 | | | 53,28 | 30,28 | | | 0,4 | 83,92 |
| Spectrum 57 | | | 59,45 | 33,92 | | | 0,29 | 93,67 |
| Spectrum 59 | | | 54,05 | 30,85 | | | 0,33 | 85,23 |

| Clinozoisite | Na2O | MgO | Al2O3 | SiO2 | CaO | MnO | FeO | WO3 | Total |
|---|---|---|---|---|---|---|---|---|---|
| Spectrum 4 | | | 32,27 | 38,63 | 23,36 | | 1,49 | | 98,94 |
| Spectrum 16 | | | 28,64 | 32,97 | 20,77 | | 1,42 | | 83,74 |
| Spectrum 17 | | | 27,76 | 33,34 | 21,43 | | 1,13 | | 83,66 |
| Spectrum 23 | | | 31,37 | 37,81 | 23,12 | | 1,31 | | 96,39 |
| Spectrum 33 | | | 32,21 | 37,6 | 24,24 | | 1,28 | | 95,56 |
| Spectrum 34 | | | 31,44 | 36,98 | 22,6 | | 1,8 | | 92,97 |
| Spectrum 35 | | | 30,94 | 36,11 | 23,24 | | 1,32 | | 91,6 |
| Spectrum 36 | | | 31,2 | 37,01 | 22,66 | | 1,75 | | 92,63 |
| Spectrum 40 | | | 31,28 | 36,86 | 23,68 | | 1,36 | | 93,18 |
| Spectrum 41 | | | 31,26 | 36,97 | 24,02 | | 1,26 | | 93,51 |
| Spectrum 42 | | | 30,52 | 36,66 | 22,23 | | 1,68 | | 91,09 |
| Spectrum 43 | | | 30,97 | 36,52 | 22,74 | | 1,72 | | 91,95 |
| Spectrum 44 | | | 30,54 | 36,19 | 23,38 | | 1,33 | | 91,43 |
| Spectrum 45 | | | 29,71 | 35,86 | 21,88 | | 2,16 | | 91,92 |
| Spectrum 56 | | | 32,22 | 38,84 | 24,74 | | 2,24 | | 98,03 |
| Spectrum 62 | | | 28,7 | 34,13 | 21,73 | | 1,37 | | 85,93 |
| Spectrum 63 | | | 28,03 | 32,53 | 20,54 | | 1,19 | | 82,27 |
| Spectrum 77 | | | 28,82 | 33,18 | 20,94 | | 1,43 | | 84,59 |
| Spectrum 102 | | | 30,78 | 35,48 | 23,26 | | 1,32 | | 90,98 |
| Spectrum 103 | | | 30,7 | 36,15 | 23,64 | | 0,82 | | 91,32 |
| Spectrum 105 | | | 30,14 | 36,12 | 22,19 | | 1,41 | | 92,81 |
| Spectrum 48 | | | 28,14 | 34,09 | 21,03 | | 1,83 | | 87,72 |
| Spectrum 58 | | | 31,38 | 37,28 | 23,6 | | 1,48 | | 93,74 |

| | | | | | | | | | |
|---|---|---|---|---|---|---|---|---|---|
| **CZO RIM** | | | | | | | | | |
| Spectrum 86 | | | 29,34 | 35,24 | 21,52 | | 1,75 | | 90,4 |
| Spectrum 88 | | | 31,15 | 36,28 | 23,08 | | 2,04 | | 92,78 |
| | | | | | | | | | |
| **CZO CORE** | | | | | | | | | |
| Spectrum 85 | | | 30,76 | 36,24 | 23,3 | | 1,3 | | 91,76 |
| Spectrum 87 | | | 31,36 | 37,09 | 23,68 | | 1,53 | | 93,66 |
| **Phengite** | **Na2O** | **MgO** | **Al2O3** | **SiO2** | **K2O** | **TiO2** | **FeO** | **BaO** | **Total** |
| Spectrum 58 | 0,94 | 1,5 | 21,88 | 32,29 | 6,39 | 0,47 | 1,14 | 0,96 | 65,57 |
| Rutile | Na2O | MgO | Al2O3 | SiO2 | CaO | TiO2 | FeO | Total | |
| Spectrum 25 | | | | | 0,24 | 99,76 | 0,3 | 100,29 | |
| **Amphibole** | **Na2O** | **MgO** | **Al2O3** | **SiO2** | **K2O** | **CaO** | **TiO2** | **FeO** | **Total** |
| Spectrum 52 | 4,82 | 11,2 | 17,68 | 43,71 | 0,81 | 9,32 | 0,21 | 12,21 | 99,95 |
| Spectrum 71 | 3,8 | 9,92 | 18,34 | 41,27 | 0,36 | 9,59 | | 12,52 | 95,81 |
| Spectrum 94 | 3,68 | 11,27 | 15,71 | 41,71 | 0,49 | 8,7 | 0,3 | 9,21 | 91,06 |
| Spectrum 98 | 3,02 | 12,32 | 16,58 | 41,21 | 0,18 | 10,95 | 0,4 | 7,51 | 92,17 |
| **Quartz** | SiO2 | Total | | | | | | | |
| Spectrum 2 | 97,83 | 97,83 | | | | | | | |
| Spectrum 15 | 102,9 | 102,9 | | | | | | | |
| Spectrum 20 | 94,62 | 94,62 | | | | | | | |
| Spectrum 37 | 96,78 | 96,78 | | | | | | | |
| Spectrum 97 | 99,67 | 99,67 | | | | | | | |
| Spectrum 104 | 93,14 | 93,14 | | | | | | | |
| Spectrum 38 | 95,83 | 95,83 | | | | | | | |
| Spectrum 50 | 97,35 | 97,35 | | | | | | | |
| Spectrum 51 | 90,87 | 90,87 | | | | | | | |

| | | | | | | | | | |
|---|---|---|---|---|---|---|---|---|---|
| Spectrum 54 | 96,47 | 96,47 | | | | | | | |
| Spectrum 56 | 101,04 | 101,04 | | | | | | | |
| **Garnet Rim** | **Na2O** | **MgO** | **Al2O3** | **SiO2** | **CaO** | **MnO** | **FeO** | **WO3** | **Total** |
| Spectrum 18 | | 10,72 | 22,5 | 39,68 | 5,7 | 0,77 | 22,57 | | 101,93 |
| Spectrum 31 | | 8,05 | 19,47 | 33,81 | 7,01 | 0,7 | 17,89 | | 86,94 |
| Spectrum 32 | | 8,29 | 19,35 | 33,84 | 6,65 | 0,68 | 18,54 | | 87,35 |
| Spectrum 47 | | 8,42 | 20,51 | 36,09 | 7,9 | 0,7 | 19,39 | | 93,02 |
| Spectrum 50 | | 7,33 | 18,73 | 33,07 | 7,06 | 0,61 | 19,53 | | 86,32 |
| Spectrum 51 | | 7,48 | 20,86 | 36,86 | 8,57 | 0,71 | 21,12 | | 95,59 |
| Spectrum 60 | | 10,19 | 21,82 | 38,06 | 5,58 | 0,64 | 21,15 | | 97,45 |
| Spectrum 66 | | 8,34 | 20,4 | 34,42 | 7,02 | 0,55 | 18,7 | | 89,43 |
| Spectrum 81 | | 9,32 | 22,57 | 39,26 | 7,52 | 0,76 | 21,29 | | 100,71 |
| Spectrum 91 | | 9,06 | 21,89 | 38,38 | 8,15 | 0,69 | 20,52 | | 98,7 |
| Spectrum 92 | | 10,02 | 20,75 | 36,87 | 5,45 | 0,71 | 20,48 | | 94,27 |
| Spectrum 96 | | 10,08 | 22,6 | 39,84 | 7,09 | 0,7 | 22,09 | | 102,4 |
| Spectrum 53 | | 9,54 | 21,43 | 37,47 | 7,13 | 0,8 | 22,58 | | 98,95 |
| **Garnet Core** | **Na2O** | **MgO** | **Al2O3** | **SiO2** | **CaO** | **MnO** | **FeO** | **WO3** | **Total** |
| Spectrum 12 | | 13,22 | 22,44 | 39,73 | 5,36 | 0,49 | 18,45 | | 99,67 |
| Spectrum 28 | | 11,95 | 20,72 | 36,54 | 5,18 | 0,42 | 16,73 | | 91,55 |
| Spectrum 29 | | 11,38 | 20,07 | 35,23 | 5,11 | 0,55 | 17,12 | | 89,46 |
| Spectrum 30 | | 10,98 | 21,07 | 36,68 | 5,36 | 0,51 | 19,43 | | 94,04 |
| Spectrum 46 | | 11,23 | 20,51 | 35,89 | 5,13 | 0,48 | 17,93 | | 91,17 |
| Spectrum 48 | | 13,58 | 23,09 | 40,42 | 7,87 | | 16,34 | | 101,53 |
| Spectrum 49 | | 12,42 | 19,71 | 34,5 | 6,78 | 0,2 | 12,22 | | 85,82 |

| | | | | | | | | | |
|---|---|---|---|---|---|---|---|---|---|
| Spectrum 59 | | 13,52 | 22,46 | 39,41 | 5,38 | 0,42 | 17,98 | | 99,16 |
| Spectrum 65 | | 12,29 | 20,93 | 37,21 | 5 | 0,44 | 17,14 | | 93,02 |
| Spectrum 70 | | 12,31 | 22,09 | 38,81 | 5,5 | 0,52 | 19,43 | | 98,66 |
| Spectrum 89 | | 12,49 | 21 | 37,13 | 5 | 0,52 | 16,78 | | 92,91 |
| Spectrum 90 | | 12,75 | 21,38 | 37,56 | 5,3 | 0,51 | 17,3 | | 94,81 |
| Spectrum 52 | | 13,79 | 22,62 | 39,7 | 5,4 | 0,45 | 20,05 | | 102,02 |

*Table B 3: Garnet pyrope-grossular-almandine components for sample SZ-N-029 normalized to 100%*

| Rim | Pyrope | Grossular | Almandine |
|---|---|---|---|
| | 29,49 | 20,22 | 50,29 |
| | 34,29 | 18,25 | 47,46 |
| | 30,10 | 21,02 | 48,87 |
| | 26,69 | 23,41 | 49,9 |
| | 27,72 | 24 | 48,28 |
| | 29,35 | 23,21 | 47,43 |
| Core | Pyrope | Grossular | Almandine |
| | 51,61 | 18,93 | 29,46 |
| | 50,25 | 19,84 | 29,91 |
| | 51,90 | 20,21 | 27,89 |
| | 50,36 | 19,25 | 30,39 |
| | 52,01 | 19,98 | 28 |
| | 51,85 | 19,58 | 28,57 |

*Table B 4: Garnet pyrope-grossular-almandine components for sample SZ-N-059 normalized to 100%*

| Core | Pyrope | Grossular | Almandine |
|---|---|---|---|
| | 48,21 | 14,05 | 37,74 |
| | 47,69 | 14,86 | 37,45 |
| | 46,15 | 14,9 | 38,95 |
| | 42,67 | 14,97 | 42,36 |
| | 44,96 | 14,76 | 40,27 |
| | 47,81 | 19,91 | 32,27 |
| | 51,43 | 20,18 | 28,39 |
| | 49,21 | 14,07 | 36,71 |
| | 48,2 | 14,09 | 37,71 |
| | 45,32 | 14,55 | 40,13 |
| | 48,99 | 14,09 | 36,92 |
| | 48,54 | 14,5 | 36,95 |
| | 47,68 | 13,42 | 38,89 |
| Rim | Pyrope | Grossular | Almandine |
| | 39,01 | 14,91 | 46,08 |
| | 34,81 | 21,79 | 43,4 |
| | 35,32 | 20,36 | 44,31 |
| | 33,71 | 22,73 | 43,55 |
| | 31,38 | 21,72 | 46,9 |
| | 29,35 | 24,17 | 46,49 |
| | 39,09 | 15,39 | 45,52 |
| | 34,93 | 21,13 | 43,94 |
| | 34,95 | 20,27 | 44,79 |
| | 34,28 | 22,16 | 43,56 |
| | 39,41 | 15,41 | 45,19 |
| | 36,56 | 18,48 | 44,95 |
| | 34,9 | 18,75 | 46,35 |